

Oscillating foils of high propulsive efficiency

By J. M. ANDERSON^{1,2}, K. STREITLIEN¹,
D. S. BARRETT¹ AND M. S. TRIANTAFYLLOU¹

¹Department of Ocean Engineering, Massachusetts Institute of Technology,
Cambridge, MA 02139, USA

²Charles Stark Draper Laboratory, Cambridge, MA 02139, USA

(Received 17 April 1996 and in revised form 17 November 1997)

Thrust-producing harmonically oscillating foils are studied through force and power measurements, as well as visualization data, to classify the principal characteristics of the flow around and in the wake of the foil. Visualization data are obtained using digital particle image velocimetry at Reynolds number 1100, and force and power data are measured at Reynolds number 40 000. The experimental results are compared with theoretical predictions of linear and nonlinear inviscid theory and it is found that agreement between theory and experiment is good over a certain parametric range, when the wake consists of an array of alternating vortices and either very weak or no leading-edge vortices form. High propulsive efficiency, as high as 87%, is measured experimentally under conditions of optimal wake formation. Visualization results elucidate the basic mechanisms involved and show that conditions of high efficiency are associated with the formation on alternating sides of the foil of a moderately strong leading-edge vortex per half-cycle, which is convected downstream and interacts with trailing-edge vorticity, resulting eventually in the formation of a reverse Kármán street. The phase angle between transverse oscillation and angular motion is the critical parameter affecting the interaction of leading-edge and trailing-edge vorticity, as well as the efficiency of propulsion.

1. Introduction

Fish and cetaceans employ their oscillating tails to produce propulsive and maneuvering forces. The tails of some of the fastest swimming animals closely resemble high-aspect-ratio foils. Because of the presumed optimal propulsive performance of fish, oscillating foils have been studied extensively using theoretical and numerical techniques (Lighthill 1975; Wu 1961, 1971; Longvinovich 1971; Cheng & Murillo 1984; Karpouzian, Spedding & Cheng 1990; McCune & Tavares 1993), and experimentally (Scherer 1968; DeLaurier & Harris 1982; Lai, Bose & McGregor 1993).

A foil in steady forward motion and a combination of steady-state harmonic heaving and pitching motion produces thrust through the formation of a flow downstream from the trailing edge, which when averaged over one period of oscillation has the form of a jet. This average jet flow is unstable, acting as a narrow-band amplifier of perturbations. The harmonic motion of the foil causes unsteady shedding of vorticity from the trailing edge, while there are conditions when leading-edge vortices form as well. The interaction between the unsteady vorticity shed by the foil and the inherent dynamics of the unstable wake result in the formation of patterns of

large-scale eddies as shown through visualization in Ohashi & Ishikawa (1972), Oshima & Oshima (1980), Oshima & Natsume (1980), and Koochesfahani (1989). The number of vortices formed per half-cycle varies with the amplitude and frequency of the motion and the shape of the waveform (Koochesfahani 1989). Triantafyllou, Triantafyllou & Gopalkrishnan (1991) have shown that optimal creation of a jet occurs at non-dimensional frequencies corresponding to the maximum spatial growth of the unstable average jet flow behind the foil, and that the propulsive efficiency reaches a maximum under these conditions. Data from the swimming characteristics of several genera of fish and cetaceans show that fish swim under the conditions of optimal efficiency (Triantafyllou, Triantafyllou & Grosenbaugh 1993). It should be noted that the shape of the time-averaged jet profile depends on the frequency and amplitude of oscillation of the foil, hence the problem must be viewed in its entirety, i.e. as a dynamic equilibrium among the interacting components, as also noted in the qualitatively similar problem of the wake of a bluff cylinder within a stream, subject to rotary oscillations (Tokumaru & Dimotakis 1991).

Linear inviscid theory predicts that an oscillating foil can reach, for certain parametric combinations, very high propulsive efficiency. Past experimental results, however, have often provided low efficiencies. Scherer (1968), for example, performed extensive tests on a foil of moderately high aspect ratio and found that the maximum efficiency is typically less than 70%. We show herein that with optimal choice of parameters, efficiency higher than 85% can be stably achieved.

Visualization results on unsteadily moving foils have been reported by a number of investigators. Freymuth (1988) studied the combined heave and pitch motions of a NACA 0015 airfoil in a wind tunnel at Reynolds numbers in the range between 5200 and 12000. Maxworthy (1979), Ellington (1984), and Freymuth (1990) studied the aerodynamics related to the flight of hovering insects and concluded that unsteady flow mechanisms play a very important role. High values of lift coefficient were associated with the formation of a leading-edge vortex, also referred to as a dynamic-stall vortex, which for specific parametric combinations was subsequently amalgamated with trailing-edge vorticity. Reynolds & Carr (1985) had provided insight earlier on the basic mechanism governing leading-edge vorticity generation. Ellington (1984) also notes the significant delay in stall caused by unsteady effects, as found earlier, for example, by Maresca, Favier & Rebout (1979) for a foil at large incidences in steady flow undergoing axial oscillations. Ohmi *et al.* (1990, 1991) studied the vortex formation in the flow around a translating and harmonically pitching foil at Reynolds numbers between 1500 and 10000, with mean incidence angle of 15° or 30° . At large incidences they found that the patterns in the vortex wake depend on whether the translational or rotational motion dominates the flow. This is determined primarily by the reduced frequency. In the case of the flow dominated by the rotational motion, the governing parameter is the product of the reduced frequency and the pitch amplitude, which is closely related to the Strouhal number of Triantafyllou *et al.* (1991, 1993). The interaction of leading-edge vortices with trailing-edge vortices determines the patterns in the wake. The Reynolds number effect was found in Ohmi *et al.* (1990) to be of secondary importance. MacCroskey (1982) provides extensive coverage of the effects of unsteady flow mechanisms on foils, including dynamic-stall vortex formation. He tends to agree that the effect of the Reynolds number on dynamic stall is small for low Mach numbers.

In this paper we present results from a series of tests to measure the forces and map the flow around a harmonically oscillating foil at zero average angle of attack. Special attention was paid to the parametric combinations that result in the optimal formation

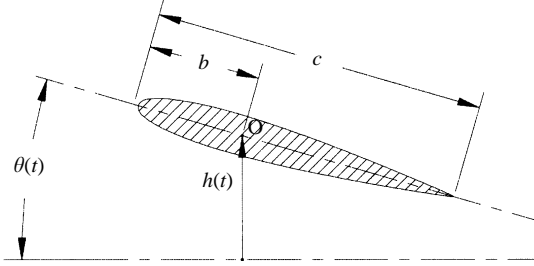


FIGURE 1. Definition of principal motion parameters, heave $h(t)$ and pitch $\theta(t)$ for an oscillating foil.

of vortical patterns. Digital particle image velocimetry was employed to visualize the flow at Reynolds number based on the foil chord of about 1100. Force measurement tests were conducted in a larger facility at Reynolds numbers of about 40 000.

2. Principal parameters of an oscillating foil

Consider, as shown in figure 1, a high-aspect-ratio foil with chord length c , moving at constant forward speed U and performing a harmonic transverse (heave) motion, $h(t)$, of amplitude h_o and frequency ω , and a harmonic angular (pitch) motion, $\theta(t)$, of amplitude θ_o and frequency ω . The pitch motion has a phase lead with respect to the heave motion, which is denoted by ψ .

Under these conditions, the foil is subject to time-varying forces $X(t)$, $Y(t)$ in the x - (forward) and y - (transverse, or lift) directions, respectively; and a torque $Q(t)$. The foil is assumed to pitch about a point O , whose distance from the leading edge is denoted by b . If T is the period of oscillation, we denote by F the time-averaged value of $X(t)$, and by P the average input power per cycle, i.e.

$$F = \frac{1}{T} \int_0^T X(t) dt, \quad (2.1)$$

$$P = \frac{1}{T} \left(\int_0^T Y(t) \frac{dh}{dt}(t) dt + \int_0^T Q(t) \frac{d\theta}{dt}(t) dt \right). \quad (2.2)$$

We define the power coefficient c_P as

$$c_P = \frac{P}{\frac{1}{2} \rho S_o U^3}, \quad (2.3)$$

and the average thrust force, F , is non-dimensionalized as follows, to provide the thrust coefficient c_T :

$$c_T = \frac{F}{\frac{1}{2} \rho S_o U^2}, \quad (2.4)$$

where ρ denotes the fluid density, and S_o denotes the area of one side of the foil, i.e. for the rectangular foil used in this study, of chord c and span s , $S_o = cs$.

The propulsive efficiency, η_P , is defined to be the ratio of useful power over input power, as

$$\eta_P = \frac{FU}{P} \quad (2.5)$$

so that $\eta_P = c_T/c_P$.

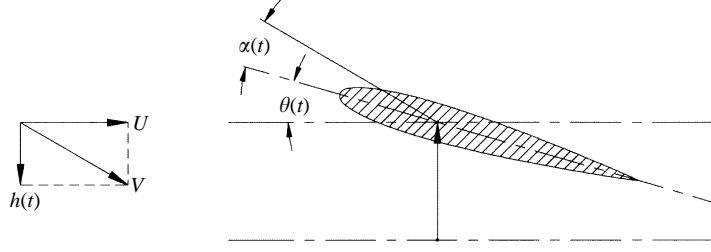


FIGURE 2. Definition of relative velocity V and nominal angle of attack $\alpha(t)$ for an oscillating foil.

There are five principal parameters in this problem, in addition to the shape of the foil (shape of cross-section, aspect ratio):

the heave amplitude-to-chord ratio $h^* = h_0/c$;

the pitch amplitude θ_0 ;

the phase angle ψ between heave and pitch (pitch leading heave);

the parameter b^* , equal to the distance of the point about which the foil pitches from the leading edge, b , divided by the chord length, i.e. $b^* = b/c$;

the non-dimensional frequency, called herein the Strouhal number St .

The Strouhal number is defined as

$$St = \frac{fA}{U}, \quad (2.6)$$

where f denotes the frequency of foil oscillation in Hz, i.e. $f = \omega/(2\pi)$, and A denotes the characteristic width of the created jet flow. Since this is unknown before measurements are made, A is taken to be equal to double the heave amplitude, i.e. $A = 2h_0$.

Alternatively, we define a Strouhal number based on the total excursion (peak to peak) of the trailing edge of the foil, A_{TE} , when we will denote it by St_{TE} :

$$St_{TE} = \frac{fA_{TE}}{U}. \quad (2.7)$$

The parameter St could be also referred to as the reduced frequency, in analogy with bluff-body wake studies. Here we follow the nomenclature of Triantafyllou *et al.* (1991), because the jet flow generated behind oscillating foils is convectively unstable, hence there is no mode competition between a natural mode and an imposed frequency, and St serves to underline the importance of this number to the instability properties of the jet flow (Triantafyllou *et al.* 1993) and hence to the vortical patterns formed.

A derivative parameter of importance to the performance of a foil is the maximum nominal angle of attack. If $\alpha(t)$ denotes the instantaneous angle of attack, referenced at the pivot point, then (figure 2)

$$\tan [\alpha(t) + \theta(t)] = \frac{1}{U} \frac{dh}{dt}(t). \quad (2.8)$$

The maximum of $\alpha(t)$ must be determined numerically and will be denoted as α_{max} . An approximation for the maximum angle of attack, denoted as α_0 , strictly valid only if the phase angle between heave and pitch is 90° , has been used primarily in the

force measurement experiments, for simplicity:

$$\alpha_o = \arctan\left(\frac{\omega h_o}{U}\right) - \theta_o. \quad (2.9)$$

In previous studies on oscillating foils two additional parameters are defined: (a) the reduced frequency, k , defined as

$$k = \frac{\omega c}{2U} \quad (2.10)$$

and (b) the feathering parameter χ :

$$\chi = \frac{\theta_o U}{h_o \omega}. \quad (2.11)$$

For large angles a better definition of this parameter, denoted by χ_L , is

$$\chi_L = \frac{\theta_o}{\arctan(h_o \omega / U)}. \quad (2.12)$$

The reduced frequency and the feathering parameter are not independent parameters. The relation between A_{TE} and the oscillating parameters is not simple, hence the expression relating k and the other parameters is not given explicitly.

In the present study we use mainly the parameters α_{max} (or α_o) and St , instead of k and χ , because of their direct relevance to the thrust coefficient and the dynamics of the wake.

3. Force and efficiency data

Experiments were conducted on a NACA 0012 foil with chord equal to 10 cm and span 60 cm, fitted with circular end plates of radius $r = 30$ cm to ensure two-dimensional flow along the major part of the foil and reduce end effects. As a result, the effective aspect ratio is larger than the nominal value of 6.

An experimental apparatus was developed, which was based on the design described in Triantafyllou *et al.* (1991, 1993). An inverted U-frame supported the foil in a horizontal position, attached to the carriage of the testing tank facility at MIT, which can run at constant speed up to 3 m s^{-1} . The tank has the following dimensions: $30 \text{ m} \times 2.5 \text{ m} \times 1.2 \text{ m}$. The foil had an average submergence of 0.6 m (mid-depth point) to minimize interference with the free surface and the bottom.

A Seiberco H3430 digitally controlled Sensorimotor and a Lintech lead-screw table provided the means for heaving the foil in harmonic motion with amplitude up to 10 cm. A second Seiberco digitally controlled Sensorimotor allowed for angular harmonic motion at arbitrary phase lead or lag with respect to the heaving motion, and with arbitrarily large pitch angle. The motion was transmitted to the foil through an arrangement of pulleys and a chain. The forces were measured with a Kistler 9117 piezoelectric transducer, placed at one end of the foil attachment, while the torque was found by measuring the force transmitted to the chain, through a second Kistler 9065 transducer. A Schaevitz linear variable differential transformer (LVDT) HR 3000 with a linear range of ± 7.62 cm was used to measure the imposed motion, and a resistance potentiometer was used to measure the angle of imposed rotation. The Kistler transducers and the Schaevitz LVDT were operated with their dedicated signal conditioners: charge amplifiers for the Kistlers and a detector/amplifier for the LVDT. The amplifiers were located on the carriage so as to be very close to the

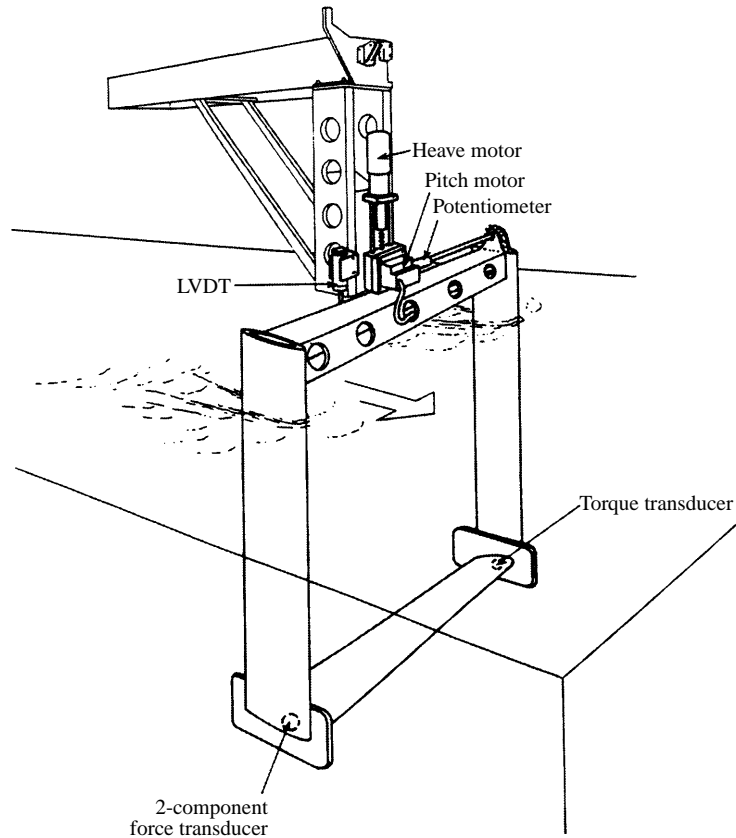


FIGURE 3. Apparatus used for conducting force measurement experiments.

sensors. The high-level analogue voltage outputs were sent to the laboratory monitor room through a connecting cable; there they were passed through a set of precision matched low-pass analogue filters to prevent aliasing. The filters were Frequency Devices four-pole Butterworth low-pass modules with a cutoff frequency of 100 Hz and specifically rigid tolerances on phase and amplitude matching.

Figure 3 provides a sketch of the experimental apparatus. The one-third-chord point was used in this study as the reference and pivot point, i.e. $b^* = \frac{1}{3}$.

We calibrated the force sensors first statically in water by hanging various weights at the mid-span of the foil, which was oriented first at 0° and then at 90° . Linearity was better than 0.1%, while repeated daily calibrations over a period of about a month provided consistent constants with no apparent drift (long-term variations of about 0.34%). We conducted dynamic calibration by oscillating the apparatus in air at ten different frequencies chosen within the range of planned test frequencies, employing three different hanging weights and measuring the forces and torque. The foil was oriented first at 0° and then at 90° . Agreement between theoretically predicted values and the data measured on the basis of static calibration was better than 2% for all frequencies and weights tested.

A single harmonic heave and pitch motion was imposed with various combinations of heave amplitude, pitch amplitude, frequency, and relative phase angle. Most tests were conducted with phase angle between heave and pitch equal to 90° , while a limited investigation was also made for the effect of the phase angle, which was

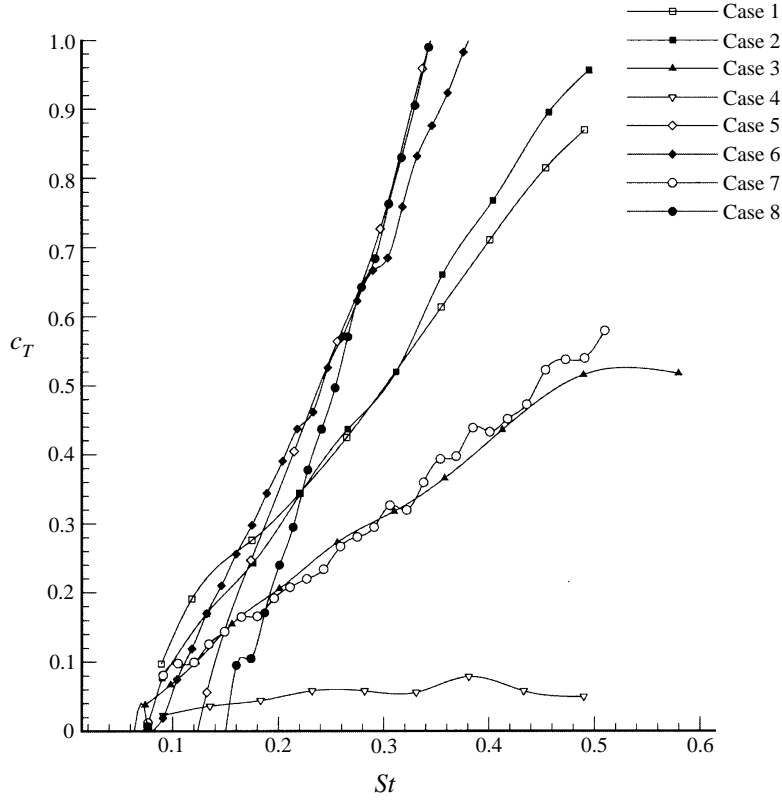


FIGURE 4. Experimentally measured thrust coefficient c_T as function of the Strouhal number St_{TE} . Curve 1: $h_o/c = 0.75$, $\alpha_{max} = 21^\circ$, $\psi = 75^\circ$; curve 2: $h_o/c = 0.75$, $\alpha_{max} = 17^\circ$, $\psi = 105^\circ$; curve 3: $h_o/c = 0.25$, $\alpha_o = 15^\circ$, $\psi = 90^\circ$; curve 4: $h_o/c = 0.75$, $\alpha_o = 5^\circ$, $\psi = 90^\circ$; curve 5: $h_o/c = 0.75$, $\alpha_o = 25^\circ$, $\psi = 90^\circ$; curve 6: $h_o/c = 0.75$, $\alpha_o = 20^\circ$, $\psi = 90^\circ$; curve 7: $h_o/c = 0.75$, $\alpha_o = 10^\circ$, $\psi = 90^\circ$; curve 8: $h_o/c = 0.75$, $\alpha_o = 30^\circ$, $\psi = 90^\circ$.

varied between 75° and 105° . For small-amplitude motions there is an equivalence between variation in the phase angle and variation in the attachment point. In the present experiments the latter was held fixed at the one-third-chord point (distance measured from the leading edge), which has some practical advantages, such as a small power required to induce the desired pitch waveform.

It was decided to perform systematic tests at a number of fixed heave amplitude-to-chord ratios: $h_o/c = 0.25$; 0.5 ; 0.75 . At each value of h_o/c tests were performed for a number of fixed nominal angles of attack, $\alpha_o = 5^\circ$; 10° ; 15° ; 20° ; 25° ; and 30° . For each combination of h_o/c and α_o , the Strouhal number was varied systematically and at small increments in the range of 0.05 and 0.60 .

Figure 4 shows the thrust coefficient c_T as function of St_{TE} for several parametric values of h_o/c and α_o , and for three different values of the phase angle ψ . Figure 5 shows the corresponding propulsive efficiency of the foil, η_P , as function of St_{TE} and for the same parametric values used in figure 4.

In selecting a propulsor to fit a given body, one imposes a condition of constant thrust and proceeds to optimize the efficiency, subject to the constant thrust constraint. While this is the proper methodology for optimizing a specific propulsor, it is not helpful to characterize the generic properties of propulsors. Our results herein are

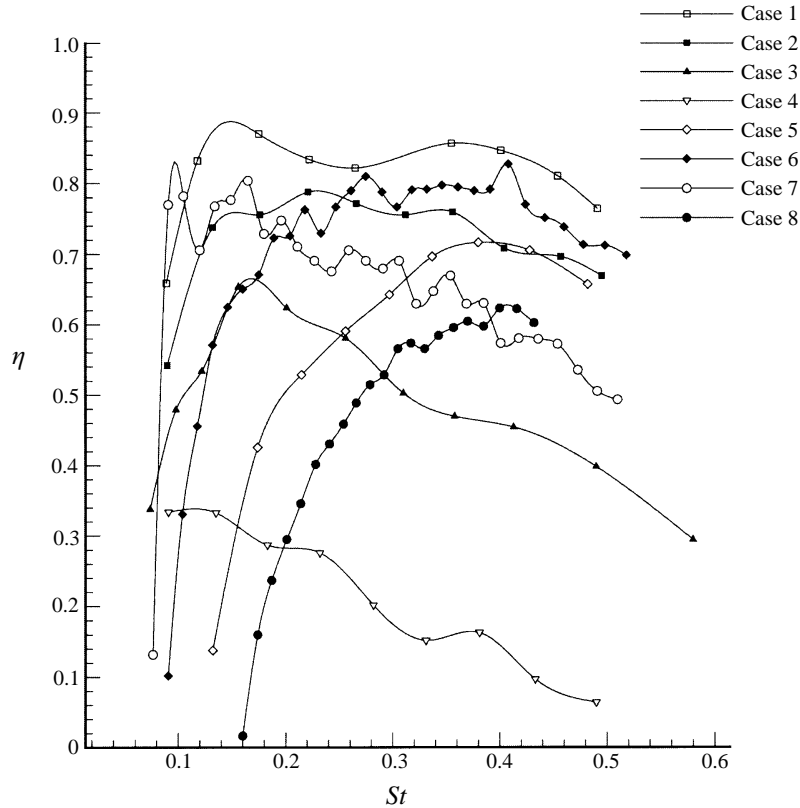


FIGURE 5. Experimentally measured efficiency as function of the Strouhal number St_{TE} . For curve identification see figure 4.

analogous to screw-propeller data, where the advance coefficient, roughly equivalent to the inverse of the Strouhal number, is varied, while the pitch-to-diameter ratio parametrizes the results, without imposing any further conditions.

The principal results of the experiments are the following:

(a) The curves of highest efficiency, obtained at constant maximum angle of attack and heave-to-chord ratio, provide typically two peaks in efficiency: one at low values of the Strouhal number St_{TE} , at about 0.15; and one at higher values of St_{TE} , in the range between the values 0.3 and 0.4. The first peak is not significant for applications because the thrust coefficient is typically very small; whereas the second peak is associated with a high thrust coefficient, of order one.

(b) At small nominal angles of attack the efficiency is poor. The highest efficiency is recorded at higher maximum angles of attack, in the range of α_o between 15° and 25° degrees.

(c) The highest efficiency is obtained when the following conditions are simultaneously met: the heave amplitude-to-chord ratio is at its highest tested value, $h_o/c = 0.75$; the phase angle between heave and pitch (pitch leading heave) is around 75° ; the max. angle of attack, α_{max} , is in the range of 15° to 25° .

(d) The highest recorded efficiency in these experiments for high thrust production was equal to 87%, and was obtained for $h_o/c = 0.75$, $\alpha_{max} = 20.2^\circ$, phase angle $\psi = 75^\circ$; and at approximately $St_{TE} = 0.36$, or $St = 0.30$

Hence, high efficiency is obtained for large heave motions and large angles of

attack. The delay of stall effects to large maximum angles of attack, due to unsteady flow effects, is in agreement with previous findings (Maresca *et al.* 1979; MacCroskey 1982). Simple actuator disk theory explains why higher amplitude motions improve efficiency, at least up to a certain threshold value: The swept-area thrust coefficient, c_{T1} , is defined as

$$c_{T1} = \frac{F}{\frac{1}{2}\rho S_1 U^2}, \quad (3.1)$$

where S_1 denotes the area swept by the trailing edge, $S_1 = sA_{TE}$. As A_{TE} increases c_{T1} decreases, resulting in higher ideal efficiency η_i , which can be shown to be (Prandtl 1952):

$$\eta_i = \frac{2}{1 + (1 + c_{T1})^{1/2}}. \quad (3.2)$$

For a given frequency, the qualitative results of the actuator disk theory are valid up to a limiting amplitude, beyond which the foil flow is characterized by simultaneous strong leading-edge and trailing-edge vortices (piston mode) providing poor efficiency.

Past experimental investigations reported mostly low propulsive efficiency of oscillating foils because the Strouhal numbers considered were well below the optimal value, and the nominal angle of attack small, presumably to satisfy linearity conditions but such conditions provide typically poor efficiency. The poor efficiency can be attributed to a mismatch between the oscillating foil parameters and the wake parameters.

Free-surface and bottom interaction effects were estimated to be insignificant for most parametric combinations, except for very high Strouhal numbers, above $St = 0.5$. Also, the apparatus had small tare friction forces and moments.

4. Comparison with numerical results

The experimental values were compared with analytical and numerical inviscid solutions. The linear theory, as given in Lighthill (1975), has been used for analytical predictions, while the numerical method given in Streitlien & Triantafyllou (1995) and Streitlien, Triantafyllou & Triantafyllou (1996) has been used to simulate the large-amplitude response of the foil. In the Appendix we provide an outline of the methodology and verification of the method.

Within linear theory it is assumed that the fluid is incompressible, inviscid and irrotational, except for the presence of a shear layer shed from the foil, and hence the flow can be described by its potential. A Kutta condition is imposed at the trailing end, and a linearized boundary condition is imposed at the average position of the foil, by assuming that the heave motion is small compared to the chord, and that the angle of attack is small. It is also assumed that the shed vorticity remains at the transverse position where it is shed by the trailing end, and is convected downstream by the average velocity of the fluid. The thrust force is of second order with respect to the perturbation parameter (which is taken to be the amplitude of motion divided by the chord length), and can be obtained in closed form for sinusoidal motion.

A numerical methodology for simulating the large-amplitude oscillating motion of a foil in an inviscid fluid is described by Streitlien & Triantafyllou (1995). The foil is assumed to have a cusp trailing-edge configuration and is mapped in the complex plane into a circle, so as to facilitate the force and moment calculation using closed-form expressions. Arbitrarily large motions can be simulated, provided there is no vorticity shed from the foil except at the trailing edge, where a Kutta condition is

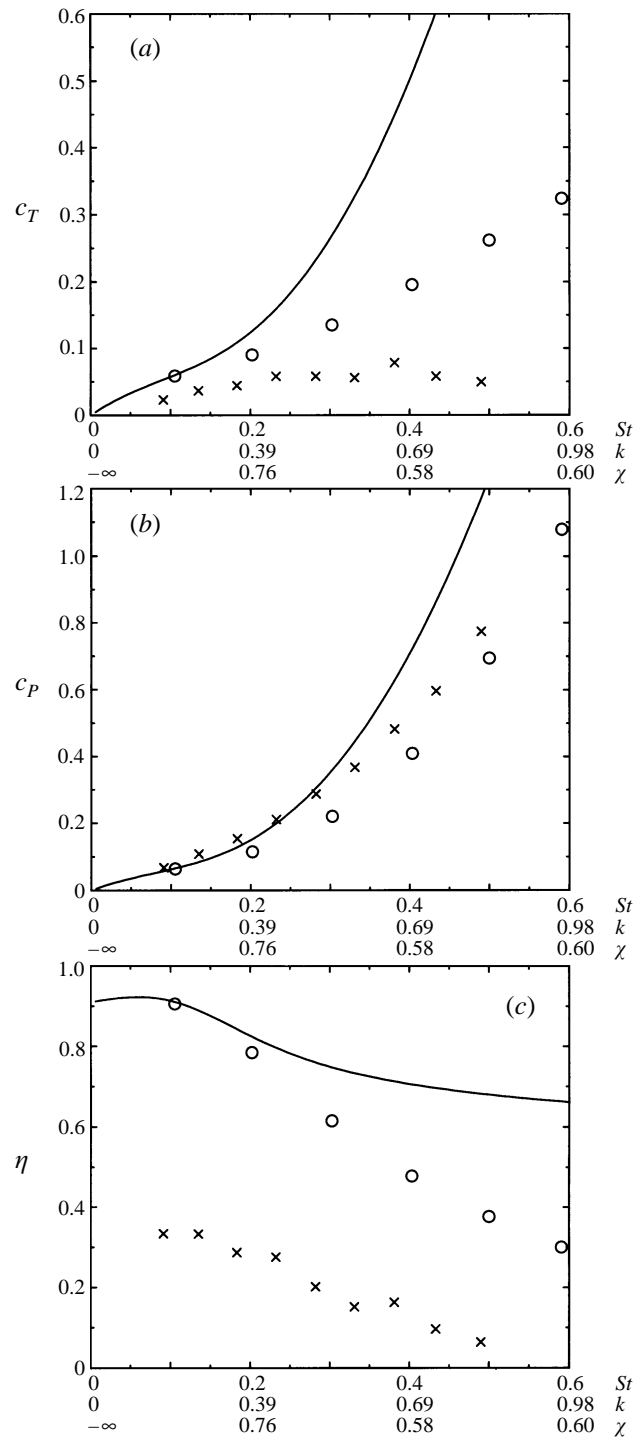


FIGURE 6. (a) Thrust coefficient, (b) power coefficient and (c) efficiency, as function of St (k and χ are also given), for $h_o/c = 0.75$, $\alpha_o = 5^\circ$, $\psi = 90^\circ$. Inviscid theory: linear (solid line) and nonlinear (o); versus experiment (\times).

assumed to hold. The self-induced dynamics of the shed vorticity are accounted for within this methodology.

Figures 6(a), 6(b) and 6(c) provide the thrust coefficient, power coefficient and the corresponding efficiency, respectively, as predicted by linear theory and nonlinear simulation, compared with the values measured experimentally for a low value of the angle of attack ($\alpha_o = 5^\circ$) and for high amplitude of motion, $h_o/c = 0.75$, and $\psi = 90^\circ$, as a function of St . The corresponding values of the parameters k and χ are also provided. It is noted that there is disagreement between linear theory, numerical simulation and experiment in thrust coefficient and efficiency, which have much lower values in the experiment. A comparison of the power coefficient shows better agreement with experiment up to Strouhal number of about 0.35; hence the disagreement lies mainly in the thrust calculation. Previous experiments have also shown that the lift and moment coefficients are well predicted by theory (Greydanus, Van de Vooren & Bergh 1952), except for very large values of the reduced frequency. The discrepancy cannot be attributed to the drag of the foil, because at higher values of St the thrust is several times larger than the value of the drag force. Nonlinear theory is somewhat closer to experiment than linear theory for higher values of St , but it is still in disagreement with experiment. The disagreement is more pronounced when small angles of attack are combined with small amplitudes of motion.

Figures 7(a), 7(b) and 7(c) provide the thrust coefficient, power coefficient and the corresponding efficiency, respectively, as function of St for a larger angle of attack, $\alpha_o = 15^\circ$, and small amplitude of motion, $h_o/c = 0.25$, and with $\psi = 90^\circ$. Agreement between theory, simulation and experiment is fair overall and the efficiency achieved is low except at low thrust levels.

Figures 8(a), 8(b) and 8(c) provide the thrust coefficient, power coefficient and the corresponding efficiency, respectively, as function of St for large angle of attack, $\alpha_o = 15^\circ$, large amplitude of motion, $h_o/c = 0.75$, and $\psi = 90^\circ$. Agreement between theory, simulation and experiment is good except at low values of St . High efficiency, of the order of 75% is achieved over a wide parametric range, including low and high levels of thrust.

Figures 9(a), 9(b) and 9(c) provide the thrust coefficient, power coefficient and the corresponding efficiency, respectively, as function of St for $\alpha_o = 15^\circ$, $h_o/c = 0.75$, but with phase angle $\psi = 75^\circ$. Agreement between theory and simulation on one hand, and experiment on the other, is good for the thrust coefficient, but the power coefficient, and hence the efficiency curves, show differences as function of St . In fact, experiment provides a lower power coefficient, and hence higher efficiency, than linear and nonlinear theory over a wide range of St . Based on the flow visualization results shown in the next section, we conclusively attribute this difference to the formation and manipulation of leading-edge vortices. This is one of the optimal cases where experiment provides very high efficiency, of the order of 85%, for a wide parametric range which includes cases of both low thrust coefficient, and high levels of thrust. The latter is especially important for applications, while, as seen from figure 9(c), the high efficiency is decreasing only slightly away from its peak value as a function of St , hence providing a stable operating condition. At maximum efficiency the maximum nominal angle, α_{max} , is calculated to be equal to 20.2° .

Finally, we compare the maximum efficiency recorded against the ideal efficiency predicted by actuator disc theory. (a) For $c_{T1} = 0.52$, which corresponds to $c_T = 0.78$, and for $St_{TE} = 0.40$ we find $\eta_i = 0.895$, while the experiments provide $\eta = 0.85$; for $St_{TE} = 0.36$ ($St = 0.30$) and $c_{T1} = 0.45$, i.e. $c_T = 0.67$, we find $\eta_i = 0.907$, while the experiments give $\eta = 0.87$.

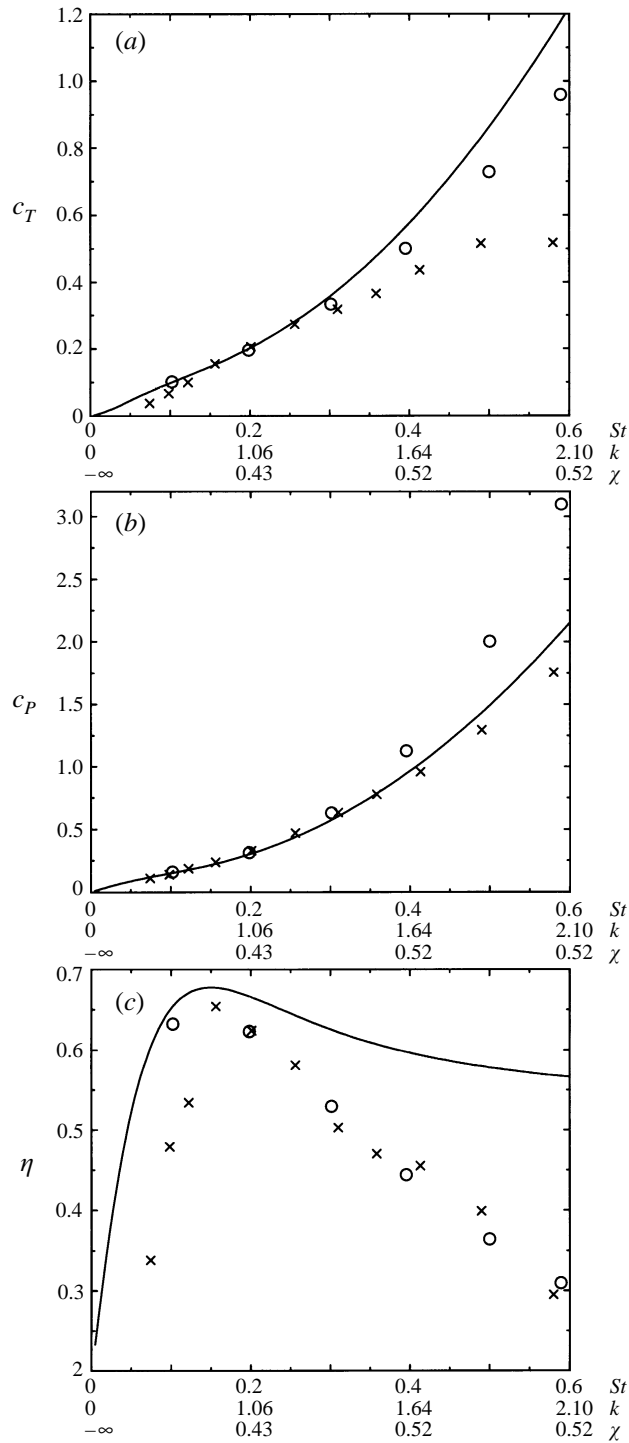


FIGURE 7. (a) Thrust coefficient, (b) power coefficient and (c) efficiency, as function of St , for $h_o/c = 0.25$, $\alpha_o = 15^\circ$, $\psi = 90^\circ$. Inviscid theory: linear (solid line) and nonlinear (o); versus experiment (x).

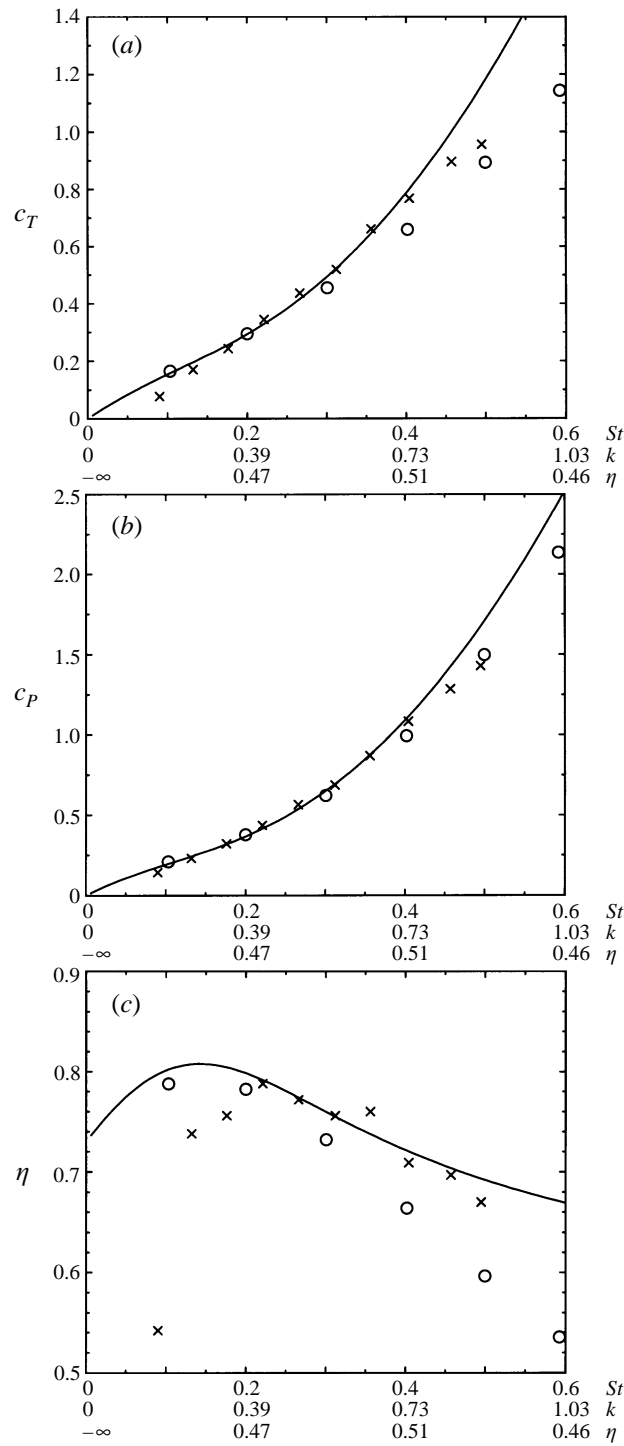


FIGURE 8. (a) Thrust coefficient, (b) power coefficient and (c) efficiency, as function of St , for $h_o/c = 0.75$, $\alpha_o = 15^\circ$, $\psi = 90^\circ$. Inviscid theory: linear (solid line) and nonlinear (\circ); versus experiment (\times).

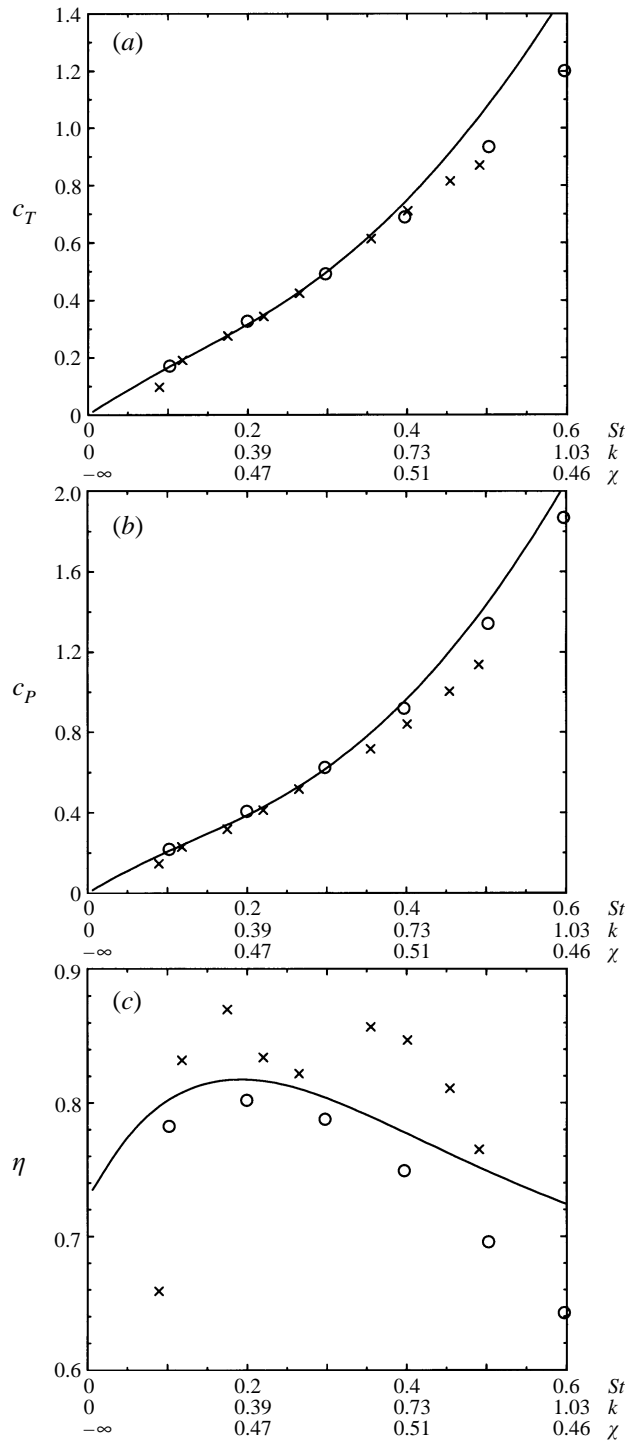


FIGURE 9. (a) Thrust coefficient, (b) power coefficient and (c) efficiency, as function of St , for $h_o/c = 0.75$, $\alpha_o = 15^\circ$, $\psi = 75^\circ$. Inviscid theory: linear (solid line) and nonlinear (\circ); versus experiment (\times).

The disagreement between inviscid theory (linear and nonlinear) and experiment is restricted to certain particular values of the parameters: it is attributed to mismatching of the foil and wake parameters, for small values of St and the angle of attack, and to the formation of leading-edge vortices which affect both the thrust and the efficiency of the foil for high values of the angle of attack and St . Since efficiency in the experiment was sometimes lower and other times higher than theory predicts, the experimental work pointed to the need for improving modelling basic flow mechanisms in the theoretical inviscid model. It was decided, therefore, to explore the flow patterns around the oscillating foil by conducting visualization experiments, which are provided in the next section.

5. Flow visualization experiments

In order to investigate the features of the flow around a oscillating foil and associate them with the measured force characteristics, visualization experiments were conducted (Anderson 1996) at smaller scale using digital particle image velocimetry (DPIV) (Willert & Gharib 1991). The flow is seeded with small light-reflecting particles and a plane is illuminated using a laser beam fanned to form a plane sheet. Image data from two successive video frames are collected and stored digitally in levels of grey-scale. In each of the frames we examine small interrogation windows at the same spatial position and the data are used to calculate the cross-correlation function which provides a goodness of match between images. A strong narrow peak in the correlation function provides the average displacement of the sampled group of particles.

We used a Texas Instruments MC-1134 camera, and observed at a video frame rate of 30 Hz. Since two frames are needed for each velocity field measurement, we obtain a 15 Hz data acquisition rate. The spatial resolution is limited by the average spacing between particles. The effect of the DPIV windowing process is that of a spatial low-pass filter. Using the analysis in Willert & Gharib (1991), we observe a 40% attenuation of features on the order of 64 pixels when a 32×32 window is used in the processing. The attenuation is limited to less than 10% for features nearing 160 pixels in size. Similarly, for a 16×16 processing window, features on the order of 32 pixels are attenuated by approximately 35%, and a 10% attenuation is realized for features near 75 pixels in size. Typically, we have a 768×480 CCD array imaging a $22 \text{ cm} \times 15 \text{ cm}$ flow cross-section, and we process with 32×32 windows and stepping increments of 8 pixels in both directions. Statistical errors near 0.01 pixels were observed for properly seeded cases, i.e. greater than 20 particles per 32×32 interrogation window. We estimate a mean relative RMS error of 5–6% for particle displacements in the range of 0–9 pixels; absolute errors ranged from 0.01 pixels to 0.15 pixels. Increased seeding densities beyond 20 particles per 32×32 window show no significant improvement in uncertainty. We can safely assume a typical relative RMS error for moderate pixel excursions (greater than 1 pixel) to be on the order of 5%. In terms of velocity this results in typical absolute error of 0.2 cm s^{-1} for a time step of 20 ms, resulting in a relative velocity error for these experiments of 7.5% (McKenna 1996).

The experiments were conducted in a specially constructed glass tank with dimensions $2.4 \text{ m} \times 0.75 \text{ m} \times 0.75 \text{ m}$. A motor-driven carriage moves along the top of the tank at constant speed, driven by an AC motor. An oscillating mechanism was mounted on top of the carriage, which allowed simultaneous heaving and pitching motion of a vertically hanging foil with various combinations of the heave and pitch amplitudes

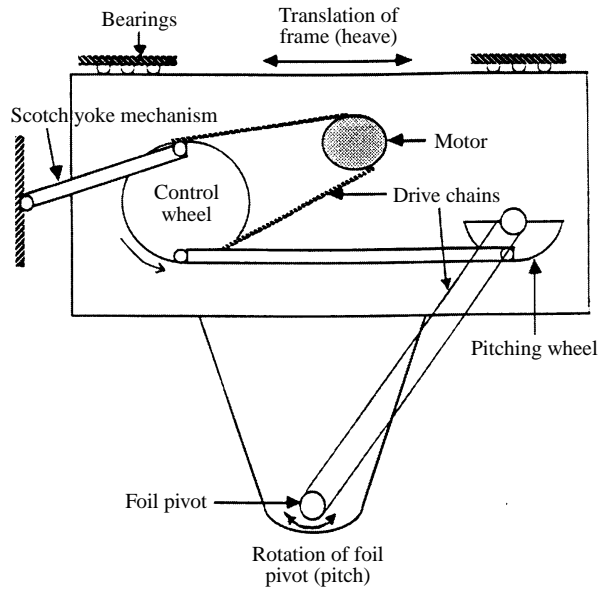


FIGURE 10. Apparatus used for conducting flow visualization experiments.

and their relative phase (figure 10). The mechanism is described in Gopalkrishnan *et al.* (1994): The heave amplitude can be varied between zero and 7.62 cm; the pitch amplitude can be set at any of the discrete settings: 0° , 7° , 15° , 30° , 45° , 60° ; and the relative phase can be set to any value. The frequency can be varied continuously from 0 to 0.7 Hz.

The foil used was a NACA 0012 foil section with chord length 3.81 cm and submerged length 71 cm, constructed by casting epoxy resin with added carbon fibre tape and with an embedded steel rod. The surface of the water was regularly skimmed and cleaned of surfactants. The Reynolds number, based on the chord length, was approximately equal to 1100.

All measurements were made in a horizontal plane at the tank mid-depth (36.2 cm from the bottom). The video camera was located horizontally below the tank looking at a mirror oriented 45° below a view-port in the tank bottom. The flow at the mid-span was two-dimensional with very low divergence, even though no end plates were fitted in order to ensure unobstructed view of the camera. The DPIV plane view was 22 cm long in the direction of foil motion and 15 cm wide. The time difference between images comprising a pair was 20 ms.

5.1. Velocity visualization data

We present results for five cases.

(1) Figure 11 shows the velocity vector plots for $St = St_{TE} = 0.10$, $h_o/c = 1$, $\theta = 7^\circ$, $\alpha_{max} = 10.4^\circ$, $\psi = 90^\circ$. The foil does not produce thrust and the wake is marginally at the state where all vortices are aligned.

(2) Figure 12(a) shows the velocity vector plots for $St = 0.30$, $St_{TE} = 0.36$, $h_o/c = 0.25$, $\theta = 15^\circ$, $\alpha_{max} = 28.3^\circ$, $\psi = 90^\circ$. A strong jet and a reverse Kármán street are produced at this frequency which provides maximum wake spatial amplification. No leading-edge vortex is observed.

(3) Figure 12(b) shows the velocity vector plots for $St_{TE} = 0.36$, $h_o/c = 0.75$, $\theta = 30^\circ$, $\alpha_{max} = 15^\circ$, $\psi = 90^\circ$. This case is similar to the previous one, except that

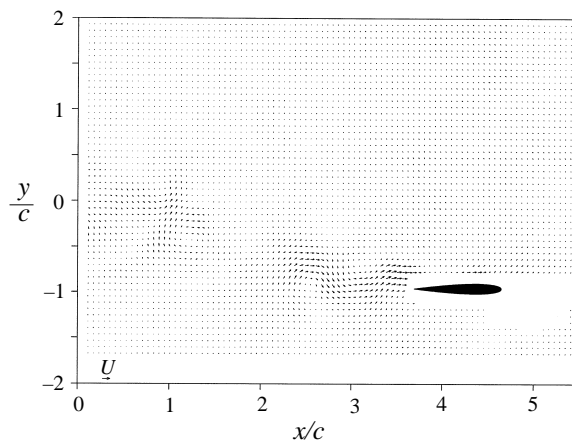


FIGURE 11. DPIV velocity data for the foil at its minimum heave position, and $St = St_{TE} = 0.10$, $h_o/c = 1.0$, $\theta = 7^\circ$, $\alpha_{max} = 10.4^\circ$, $\psi = 90^\circ$.

the amplitude of oscillation is three times higher. A very strong jet results and a leading-edge vortex is formed, but the resulting wake is quite similar to the previous case (2). We use this case as a basis for comparison with the next two cases.

(4) Figure 12(c) shows the velocity vector plots for $St_{TE} = 0.36$, $h_o/c = 0.75$, $\theta = 30^\circ$, $\alpha_{max} = 20.4^\circ$, $\psi = 75^\circ$. The only difference with respect to case (3) is the phase angle which has been reduced to 75° , resulting also in a higher angle of attack. A stronger leading-edge vortex forms which is convected towards the trailing edge, where it coalesces with vorticity shed by the trailing edge to form strong vortices which create a reverse Kármán street. This phase angle was found to be ideal for optimizing the efficiency of the foil in the force measurement experiments. As seen from figure 12(c), the foil is favourably inclined when the leading-edge vortex has formed to create thrust from the suction produced by the vortex.

(5) Figure 12(d) shows the velocity vector plots for $St_{TE} = 0.36$, $h_o/c = 0.75$, $\theta = 30^\circ$, $\alpha_{max} = 20.2^\circ$, $\psi = 105^\circ$. Again, the primary difference between this case and case (3) is the different phase angle, and the resulting larger angle of attack. Although the basic characteristics of the flow are similar to those observed in case (4), i.e. leading-edge vortex formation leading to the formation of a reverse Kármán street, the propulsive efficiency is lower, because the stall vortex sheds later in the oscillation cycle when it is unfavourably positioned on the downstream-facing side of the foil.

Figure 13 shows a composite of twelve velocity vector plots taken sequentially at equidistant intervals within half a period of oscillation, and for the same parameters as in figure 12(c), i.e. under conditions of optimal efficiency. The laser beam has been repositioned in this particular set of experiments to face the lower foil side, in order to illustrate the formation, evolution and eventual interaction of the leading-edge vortex forming on that side with trailing-edge vorticity, to form a reverse Kármán street. The results of the visualization suggest that inviscid theory predictions may be improved to cover large-amplitude motions by modelling the leading-edge vortex formation, using, for example, the methodology demonstrated by Katz (1981).

5.2. Thrust estimate from DPIV data

In order to obtain a quantitative comparison between the DPIV data and the force measurement data, given that they were performed at different Reynolds numbers,

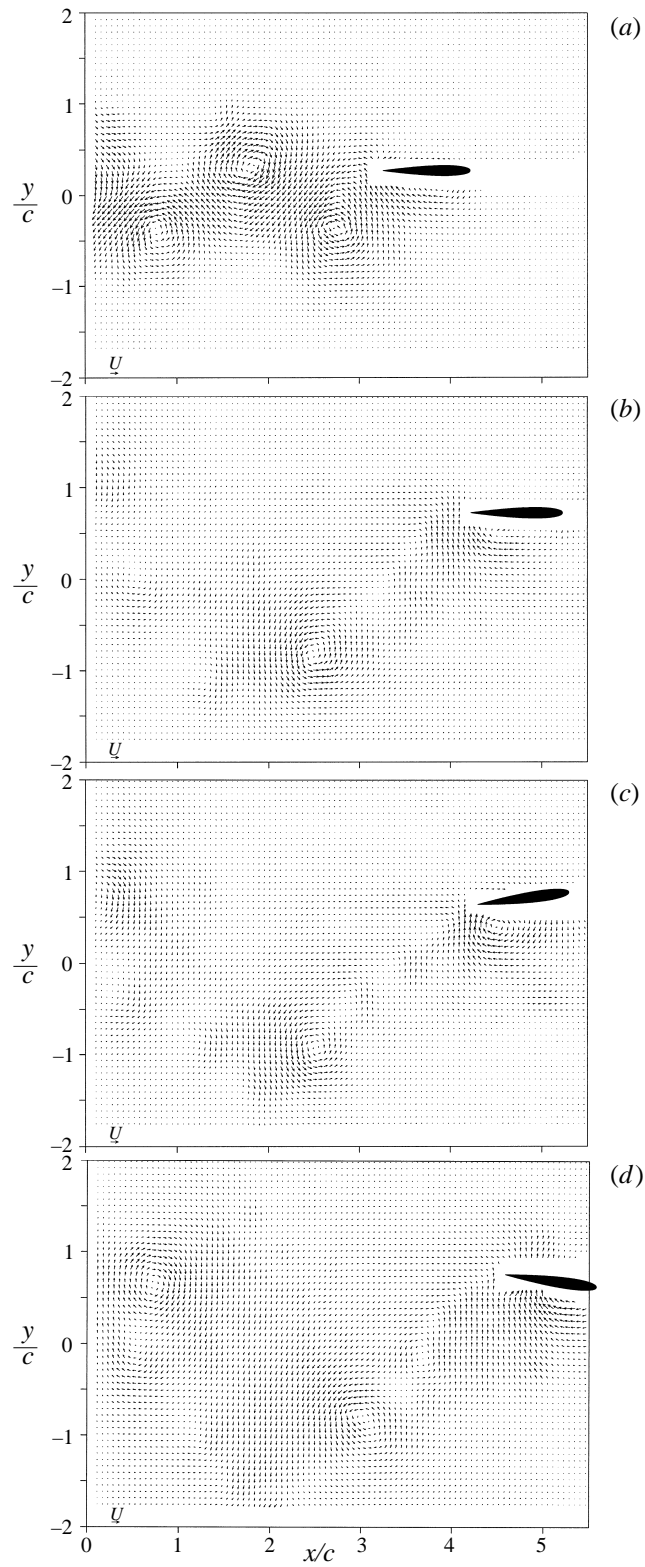


FIGURE 12. For caption see facing page.

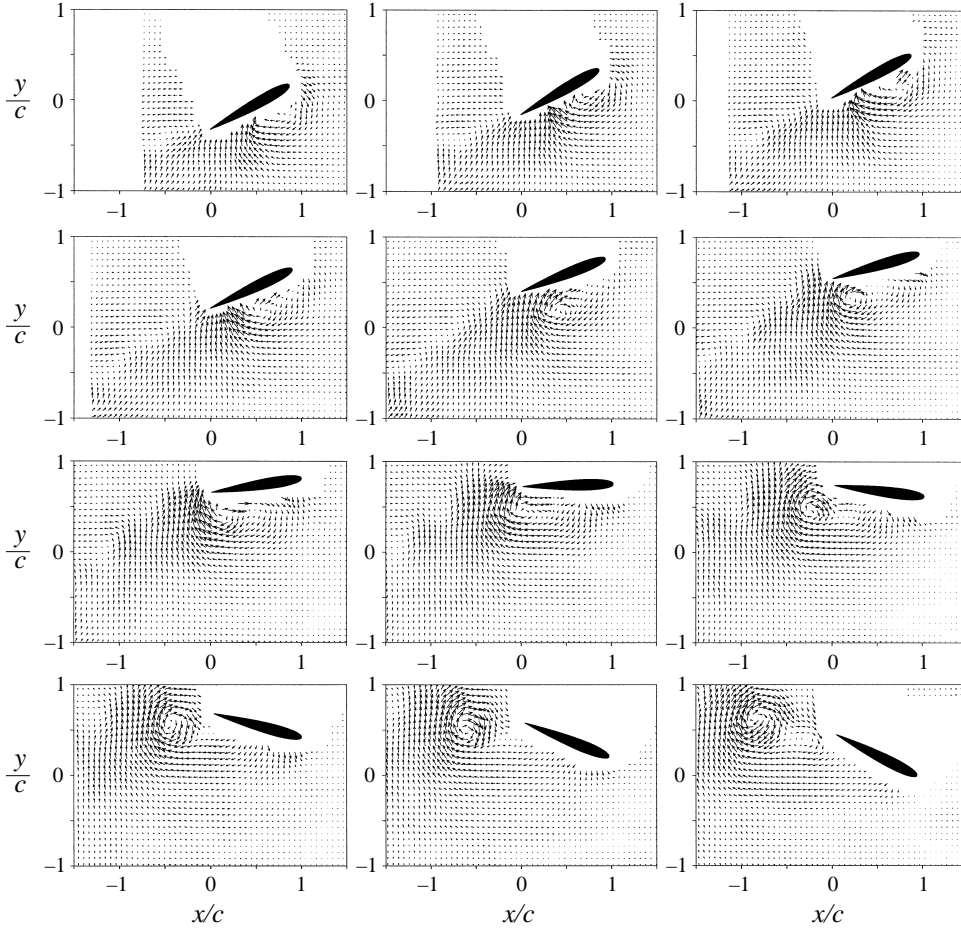


FIGURE 13. Leading-edge vortex development sequence for $St_{TE} = 0.32$, $h_o/c = 0.75$, $\theta = 30^\circ$, $\psi = 75^\circ$. Sequence starts in upper left corner at $t^* = t/T = 0$, proceeds from left to right, top to bottom in increments $\Delta t^* = 0.042$.

an average thrust force estimate was obtained, using the wake excess velocity and the momentum theorem expressed for a control volume \mathcal{V} bounded by a control surface \mathcal{S} (Batchelor 1967). We chose to calculate the average thrust, because DPIV velocity data are not available in certain locations due to shadows cast by the moving foil, while close to the foil surface data are unavailable due to the contamination of the image data by the unsteadily moving foil. Hence, we used the momentum theorem in its time-averaged form.

Consider the control volume $ABCD$ fixed to the foil in figure 14. At the upstream boundary BC , the velocity across the boundary is the towing velocity U . At the downstream position AD , the velocity across the boundary is $u(y)$, referenced to inertial coordinates.

FIGURE 12. DPIV velocity data for the foil at its maximum heave position, and (a) $St = 0.30$, $St_{TE} = 0.36$, $h_o/c = 0.25$, $\theta = 15^\circ$, $\alpha_{max} = 28.3^\circ$, $\psi = 90^\circ$; (b) $St_{TE} = 0.36$, $h_o/c = 0.75$, $\theta = 30^\circ$, $\alpha_{max} = 15^\circ$, $\psi = 90^\circ$; (c) $St = St_{TE} = 0.36$, $h_o/c = 0.75$, $\theta = 30^\circ$, $\alpha_{max} = 20.4^\circ$, $\psi = 75^\circ$; (d) $St_{TE} = 0.36$, $h_o/c = 0.75$, $\theta = 30^\circ$, $\alpha_{max} = 20.2^\circ$, $\psi = 105^\circ$.

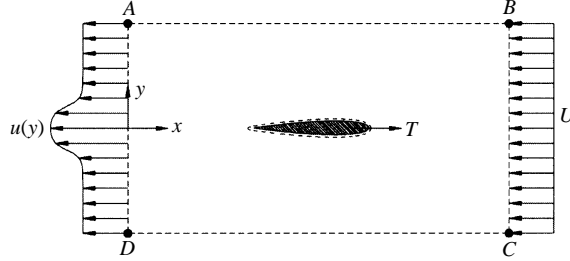


FIGURE 14. Control volume for momentum analysis

Under the assumption of steady (time-averaged) flow, and that the pressure is constant along the control volume boundaries, the thrust on the foil T can be written in terms of the flux of momentum in the x -direction as

$$T = -F_x = \rho \int_{-\infty}^{\infty} U^2 - u(y)^2 dy. \quad (5.1)$$

If we apply mass conservation, then equation (5.1) simplifies to

$$T = \rho \int_{-\infty}^{\infty} u(y)(u(y) - U) dy. \quad (5.2)$$

The average wake velocity excess in the streamwise direction is calculated by averaging twenty slices of the wake spanning one wavelength behind the trailing edge, at one instant in time. When the wavelength of the motion is larger than the experimental view, two or more snapshots of a portion of the wake are averaged. In all cases, we use whole multiples of the spatial wavelength. The accuracy of the averaging technique was verified by comparison with calculations in which the number of slices was doubled and then tripled. Further comparison with duplicate runs showed that the average velocity excess is accurate and repeatable to within 2%.

Tables 1 and 2 summarize quantitative results for thirty-five visualization experiments, subdivided into nine groups, numbered I to IX. We list the principal parameters, namely St , St_{TE} , the reduced frequency κ , θ_o , ψ , α_{max} , the feathering parameter χ ; and we include Ω_{max}^* , defined in terms of the rate of change of the angle of attack, $\dot{\alpha} = d\alpha(t)/dt$, as

$$\Omega_{max}^* = \max \left(\left| \frac{\dot{\alpha}c}{2U} \right| \right); \quad (5.3)$$

Ω_{max}^* provides a measure of the rate of change of the angle of attack.

Also we provide the average maximum velocity defect in the wake $|\overline{u - U}/U|_{max}$, the qualitative description of the leading-edge vortex, the non-dimensional circulation in the wake vortices $\Gamma_{wake}^* = \Gamma_{wake}/(U c)$, the non-dimensional circulation in the leading-edge vortex (dynamic stall vortex), $\Gamma_{DSV}^* = \Gamma_{DSV}/(U c)$, and the average thrust coefficient, c_f .

The circulation of the wake vortices is measured for a vortex approximately half a wavelength downstream from the trailing edge. Both circulations are calculated through integration along a circular path with the smallest radius yielding a convergent value or 1.5 cm, whichever is smaller. There are two sources of error affecting the repeatability of the calculation: the approximation in locating the centre of a vortex, resulting in an error of less than 5%; and small differences in the age of the vortex, providing an error of less than 3%. In a few cases, when the wake is highly mixed,

Group	Case	$\frac{St}{2h_o f}$	St_{TE}	$\frac{k}{\pi f c}$	$\frac{h_o}{c}$	θ_o (deg.)	ψ (deg.)	α_{max} (deg.)	χ	$\frac{\Omega_{max}^*}{2U} _{max}$
I	1	0.10	0.10	0.16	1.0	0	90	17.4	0	0.05
	2	0.10	0.10	0.16	1.0	7	90	10.4	0.39	0.03
	3	0.10	0.10	0.16	1.0	15	90	2.4	0.83	0.01
II	1	0.15	0.15	0.24	1.0	0	90	25.2	0	0.11
	2	0.15	0.15	0.24	1.0	7	90	18.2	0.26	0.08
	3	0.15	0.15	0.24	1.0	15	90	10.2	0.56	0.05
III	1	0.30	0.30	0.47	1.0	7	90	36.3	0.13	0.39
	2	0.30	0.30	0.47	1.0	15	90	28.3	0.28	0.32
	3	0.30	0.32	0.47	1.0	30	90	13.3	0.56	0.20
IV	1	0.45	0.48	0.71	1.0	30	90	24.8	0.37	0.63
	2	0.45	0.51	0.71	1.0	45	90	13.3	0.56	0.44
	3	0.45	0.54	0.71	1.0	60	90	5.3	0.74	0.26
V	1	0.1	0.10	0.63	0.25	0	90	17.4	0	0.20
	2	0.3	0.36	1.88	0.25	15	90	28.3	0.28	1.28
	3	0.45	0.76	2.83	0.25	30	90	24.8	0.37	2.50
VI	1	0.1	0.10	0.31	0.5	0	90	17.4	0	0.10
	2	0.3	0.32	0.94	0.5	15	90	28.3	0.28	0.64
	3	0.45	0.55	1.41	0.5	30	90	24.8	0.37	1.25
VII	1	0.45	0.33	0.71	1.0	30	30	52.7	0.37	0.82
	2	0.45	0.37	0.71	1.0	30	50	42.4	0.37	0.72
	3	0.45	0.42	0.71	1.0	30	70	32.2	0.37	0.65
	4	0.45	0.48	0.71	1.0	30	90	24.8	0.37	0.63
	5	0.45	0.48	0.71	1.0	30	100	28.0	0.37	0.63
	6	0.45	0.48	0.71	1.0	30	105	30.0	0.37	0.64
	7	0.45	0.52	0.71	1.0	30	110	32.2	0.37	0.65
VIII	1	0.45	0.24	1.41	0.5	30	30	52.7	0.37	1.65
	2	0.45	0.35	1.41	0.5	30	50	42.4	0.37	1.44
	3	0.45	0.45	1.41	0.5	30	70	32.2	0.37	1.30
	4	0.45	0.55	1.41	0.5	30	90	24.8	0.37	1.25
	5	0.45	0.55	1.41	0.5	30	100	28.0	0.37	1.27
	6	0.45	0.55	1.41	0.5	30	105	30.0	0.37	1.28
	7	0.45	0.62	1.41	0.5	30	110	32.2	0.37	1.30
IX	1	0.32	0.35	0.67	0.75	30	90	15.2	0.52	0.32
	2	0.32	0.31	0.67	0.75	30	75	20.4	0.52	0.34
	3	0.32	0.38	0.67	0.75	30	105	20.4	0.52	0.34

TABLE 1. Summary of foil experiment cases, $R_c = 1100$. St and St_{TE} are the Strouhal numbers based on heave double amplitude and trailing-edge excursion respectively.

as for example in the case of multiple vortices per half-cycle, the overall deviation increases to about 15%.

Groups I and II provide qualitative results for the wake for low Strouhal numbers when little or no thrust is produced. The wake is undulating but no distinct vortices can be discerned; a weak leading-edge vortex appears for higher values of the angle of attack.

Groups III and IV provide data for $h_o/c = 1$ and two Strouhal numbers, $St = 0.30$ and $St = 0.45$, respectively. This is a range in St of high thrust production, while stable reverse Kármán streets form except for very high angles of attack. The general trend is that wake and leading-edge vortices have increased circulation as the angle

Group	Case	$\left \frac{u-U}{U} \right _{max}$	l.e. sep	Γ_{wake}^*	Γ_{DSV}^*	c_f
I	1	-	4	-	-	-
	2	-	None	-	-	-
	3	-	None	-	-	-
II	1	-	2	-	-	-
	2	-	2	-	-	-
	3	-	Weak 4	-	-	-
III	1	0.37	1, 3	2.0	2.5	1.04
	2	0.24	1, 3	1.8	1.4	1.20
	3	-	4	0.9	0.7	0.28
IV	1	0.36	1	2.0	1.3	2.98
	2	0.29	1	1.3	1.6	1.95
	3	-	None	-	-	-
V	1	-	Weak 4	-	-	-
	2	0.40	2	1.4	-	0.77
	3	1.12	None	2.4	-	2.93
VI	1	-	2, 3	-	-	-
	2	0.39	1	1.3	0.9	1.16
	3	0.69	1	1.6	1.5	1.86
VII	1	0.18	1	2.4	2.8	-0.04
	2	0.38	1,3	2.2	2.8	0.85
	3	0.35	1,3	2.0	1.9	1.78
	4	0.36	1	2.0	1.3	2.98
	5	0.32	1	1.5	1.2	2.09
	6	0.34	1	1.5	1.4	2.68
	7	0.36	1,3	1.9	-	2.59
VIII	1	-	1	-	-	-
	2	0.53	1	1.9	1.2	0.97
	3	0.36	1	1.5	1.2	0.94
	4	0.69	1	1.6	1.5	1.86
	5	0.73	1	2.0	-	3.37
	6	0.68	1	2.2	-	2.72
	7	0.81	Weak 2	2.3	-	3.55
IX	1	0.15	1	1.1	1.3	0.70
	2	0.13	1	0.9	1.1	0.34
	3	0.17	1	1.0	1.1	0.77

TABLE 2. Summary of foil experiment results, $R_c = 1100$. Dynamic-stall vortex: (1) well separated vortex rolls along body, (2) less-organized separated vortex rolls along body, (3) secondary leading-edge vortices present, (4) separated region, does not roll up until trailing edge.

of attack and St increase, but the quantitative trends differ with St and α_{max} : for $St = 0.30$, which theory predicts to be in the optimal thrust producing range, an increase of the angle of the attack from 13.3° to 24.8° (cases III-2 and III-3) provides a corresponding doubling of the circulations Γ_{wake}^* , Γ_{DSV}^* , and a quadrupling of the thrust force. A similar increase in the angle of attack for $St = 0.45$ (cases IV-1 and IV-2) causes a substantial increase in the circulation of the wake vortices but not in the leading-edge vortex. For angle of attack equal to 13.3° , an increase from $St = 0.3$ to $St = 0.45$ causes a substantial increase in both vortices; this does not happen for a larger angle of attack (cases III-2 and IV-1).

Group V provides data for the lowest heave amplitude, $h_o/c = 0.25$, and three

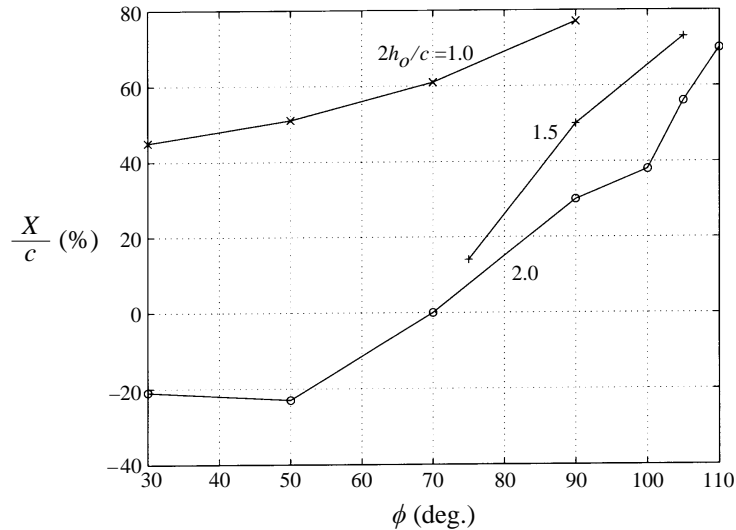


FIGURE 15. Leading-edge vortex location along the foil at the position of maximum heave motion as a function of phase angle (see table 2, groups VII, VIII, IX).

Strouhal numbers. A weak or no leading-edge vortex appears, since the heave motion is relatively small and pitch effects dominate as observed by Ohmi *et al.* (1990, 1991) and Visball & Shang (1989). In contrast, the wake vortices retain a comparable circulation for the same angle of attack as for $h_o/c = 1$.

Group VI provides data for the intermediate heave amplitude, $h_o/c = 0.5$, and three Strouhal numbers. One again finds comparable strength of the wake vortices as for group V, but the leading-edge vortex has strengthened to values comparable to those at $h_o/c = 1$.

Groups VII and VIII provide the dependence of the foil and wake characteristics on the relative phase between heave and pitch for h_o/c equal to 0.5 and 1, respectively. The phase angle is varied systematically between 30° and 110° . The maximum angle of attack varies as function of the phase angle, in the range between 28° and 53° ; this is reflected in the circulation of the wake and leading-edge vortices, as well as in the thrust coefficient. Figure 15 shows the position of the leading-edge vortex along the foil chord, measured from the trailing edge (positive towards the leading edge), for three different heave-to-pitch ratios (groups VII, VIII, IX in table 1), as function of the phase angle between heave and pitch, ψ . The significant effect of the phase angle on the location of the leading-edge vortex is clearly shown.

In summary, the leading-edge vortex intensifies with h_o/c and the angle of attack, and its position and subsequent interaction with trailing-edge vorticity is governed by the phase angle ψ .

Group IX provides results for $h_o/c = 0.75$, $St = 0.32$ and three values of the phase angle $\psi = 90^\circ, 75^\circ, 105^\circ$. These results are directly comparable with the force-measuring experiments, since all principal parameters are almost the same; the comparison is provided in table 3. The agreement in thrust coefficient between the two sets of experiments is good considering the approximate methodology used with the DPIV data.

The effect of h_o/c is apparent when considering cases V-2, VI-2 and III-2: the Strouhal number (0.3), and the angle (28.3°) are the same for all three cases. For V-2

Case	ψ (deg.)	α_{max} (deg.)	c_T	α_{max}^* (deg.)	c_T^*
1	90	15.2	0.70	15	0.67 ⁽¹⁾
2	75	20.4	0.34	21	0.52
3	105	20.4	0.77	17	0.74

TABLE 3. Calculated thrust coefficient from DPIV data, c_T , versus measured thrust coefficient, c_T^* . All cases for $St = 0.32$ and $h_o/c = 0.75$ (Group IX). ⁽¹⁾: Data obtained by interpolation.)

($h_o/c = 0.25$) there is no leading-edge vortex while $\Gamma_{wake}^* = 1.4$, resulting in $c_f = 0.77$. For VI-2 ($h_o/c = 0.5$) $\Gamma_{DSV}^* = 0.9$ and $\Gamma_{wake}^* = 1.3$, resulting in $c_f = 1.16$. For III-2 ($h_o/c = 1$) $\Gamma_{DSV}^* = 1.4$ and $\Gamma_{wake}^* = 1.8$, resulting in $c_f = 1.20$.

The additional parameters given in table 1, i.e. k , χ and Ω_{max}^* , can also be combined to describe the features of the flow; for our purposes, i.e. the characterization of the vortical structures in the wake and the strength and position of the dynamic-stall vortex, we find, in order of importance, (a) the Strouhal number and the angle of attack, (b) the heave to chord ratio, and (c) the pitch to heave phase angle, to be the most pertinent set of parameters.

5.3. Leading-edge vortex and wake form

The formation of leading-edge vortices and the formation of a reverse Kármán street is closely associated with the maximum propulsive efficiency found in our experiments. Freymuth (1988) studied the combined heave and pitch motions of a NACA 0015 airfoil and at the equivalent values of $St = 0.34$ and $h_o/c = 0.2$ he observed the formation of a reverse Kármán street. He found for pitching motion about the quarter-chord point and angles of attack about 20° that a weak leading-edge vortex forms, which is convected downstream and merges with trailing-edge vorticity. Maxworthy (1979) and Ellington (1984) also found in the study of hovering insects that leading-edge bubbles form, eventually forming a street of vortices in the wake.

For a given amplitude-to-chord ratio h_o/c , leading-edge vortices are formed when the angle of attack exceeds a threshold value. We provide two additional figures to cover a wider range in the angle of attack and St . Figure 16(a) shows the flow for high Strouhal number and moderate angle of attack. The flow corresponds to the foil being at its lowest heave position, for $St_{TE} = 0.50$, $h_o/c = 1$, $\theta_o = 45^\circ$, $\alpha_{max} = 13.3^\circ$, $\psi = 90^\circ$. A well-organized leading edge vortex is present, while in the wake four vortices per cycle are present.

Figure 16(b) shows the flow for moderate Strouhal number and high angle of attack. The foil is at its highest heave position for $St_{TE} = 0.33$, $h_o/c = 1$, $\theta_o = 30^\circ$, $\alpha_{max} = 52.7^\circ$, $\psi = 30^\circ$. A very strong leading-edge vortex forms and is shed well before the foil reaches the maximum heave excursion, while the wake consists of four vortices per cycle, resulting in a piston-like mode of response.

Figure 17 summarizes the observational data on the flow around oscillating foils for the cases reported in table 1, as well as other visualization data conducted with the same apparatus at $h_o/c = 1$, as function of the angle of attack and the Strouhal number.

We distinguish several regions. In regions A and B ($St < 0.2$) the wake does not roll up into discrete vortices; in region B a very weak leading-edge vortex appears for $\alpha_{max} > 30^\circ$, but the wake retains its wavy form. For angles of attack larger than

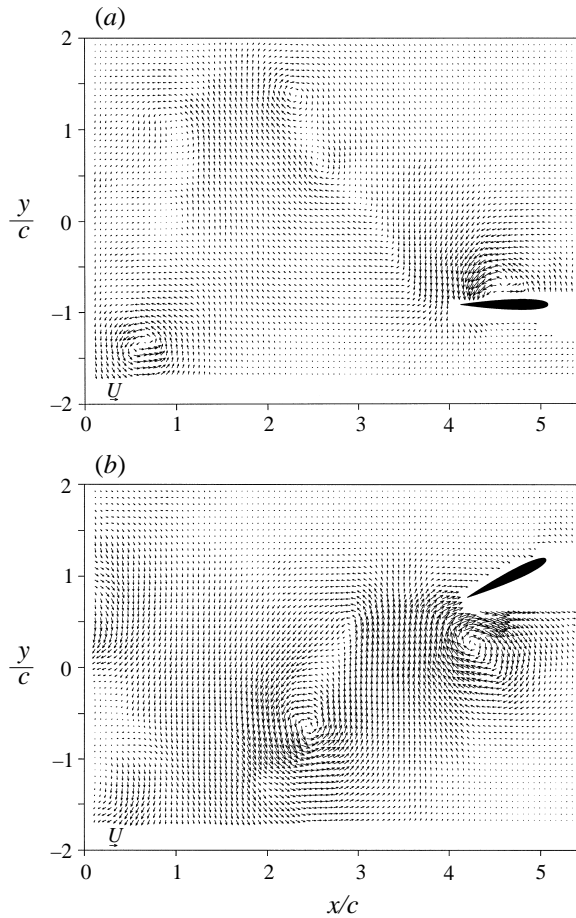


FIGURE 16. DPIV velocity data for the foil at its minimum heave position, and (a) $St_{TE} = 0.50$, $h_o/c = 1$, $\theta = 45^\circ$, $\alpha_{max} = 13.3^\circ$, $\psi = 90^\circ$; (b) $St_{TE} = 0.33$, $h_o/c = 1$, $\theta = 30^\circ$, $\alpha_{max} = 52.7^\circ$, $\psi = 30^\circ$.

about 50° a ‘piston’ mode appears where leading- and trailing-edge vortices form and roll up in the wake to form four vortices per cycle. In region E, for angles of attack smaller than 5° , the wake does not form distinct patterns. Region C, contained in the limits $7^\circ < \alpha_{max} < 50^\circ$ and $0.2 < St < 0.5$, is characterized by the formation of a clear reverse Kármán street. A leading-edge vortex forms for angles of attack larger than about 10° , increasing in strength with increasing angle of attack, which is amalgamated with trailing-edge vortices to form two vortices per cycle. Region D ($St > 0.5$) is characterized by the formation of leading-edge vortices, which interact with trailing-edge vorticity to form four vortices per cycle. Data for lower h_o/c show nearly identical trends as far as the wake form is concerned; the formation of a leading-edge vortex depends on h_o/c , however.

In studies of a foil oscillating harmonically in heave and/or pitch motion, Ohashi & Ishikawa (1972) and Oshima & Oshima (1980) provide figures classifying the vortical patterns forming in the wake. The plots are provided as function of two parameters, which correspond to $k = \omega c/U$ and $h^* = h_o/c$ herein, the product of which equals $kh^* = \pi St$; hence values of constant St should appear as hyperbolae in their graphs. In figure 8 of Ohashi & Ishikawa (1972) the appearance of a reverse Kármán street

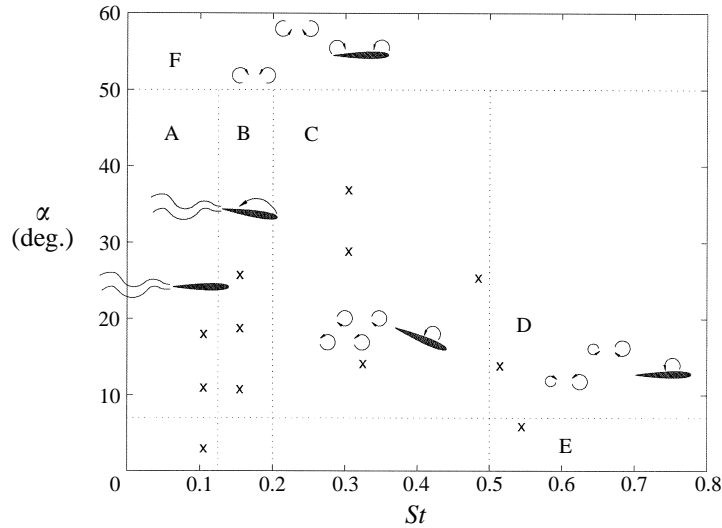


FIGURE 17. Wake patterns as function of the Strouhal number and angle of attack for $h_o/c = 1$. Points mark the location of experiments reported in table 1.

is marked for an area lying above a curve closely resembling a hyperbola and corresponding to a value of St between 0.2 and 0.25, below which a ‘wavy wake’ is noted. In figure 1 of Oshima & Oshima (1980) similar curves are plotted: a reverse Kármán street is noted to appear at $St \approx 0.25$; a hyperbola corresponding to $St \approx 0.5$ marks the appearance of a ‘strong mixing wake’, which consists of four vortices per cycle. The agreement with results herein is very close.

Figure 17 demonstrates the significance of the Strouhal number on the form of the wake, as predicted by the theory of Triantafyllou *et al.* (1991, 1993). The presence of a leading-edge vortex is strongly influenced by the angle of attack. In region C, for St between 0.2 and 0.5, strong thrust develops from a reverse Kármán street (see table 2), accompanied by up to a moderately strong leading-edge vortex. Region C contains the region of optimal efficiency found in the force experiments. In region D, for St larger than 0.5, strong thrust develops accompanied by the formation of two vortices per half-cycle, which have opposite circulation and, in general, different strength. Regions A and B are characterized by low or negative thrust, and a wavy wake with no distinct vortex formation; the leading-edge vortex is very weak. In region E, for very small angles of attack, very small or negative thrust develops.

5.4. Three-dimensional effects

The experiments to measure force were conducted with attached end plates, having a radius equal to three times the chord length. Hence the effective aspect ratio was larger than the span-to-chord ratio $s/c = 6$. In force measurement experiments with oscillating bluff cylinders using the same apparatus (Gopalkrishnan *et al.* 1994), forces became independent of the ratio of end-plate diameter to cylinder diameter, D/d , when $D/d > 5$ and the span-to-diameter ratio was larger than 5. Szepessy & Bearman (1992) also show that forces on stationary cylinders with diameter d in steady cross-flow become independent of the span-to-diameter ratio s/d when $s/d > 5$. They used slightly larger end plates than used in this study (rectangular end plates $7d$ by $8d$) and they covered a wide Reynolds number range. In the present tests the symmetry of the end plates causes the flow in the middle cylinder sections to be nearly planar,

although some differences must be expected with respect to the infinite span case. In the DPIV tests three-dimensional effects do not significantly affect the flow in the near wake due to the high aspect ratio of the foil ($AR = 18.6$) and the strong correlation of the vortices with the foil motion. The visualization data were acquired at the foil mid-span where the flow is least affected by free-surface and foil-end effects. The foil free end was very close to the tank bottom (approximately $8\% c$). Dye visualization showed that with this clearance the end effects are significantly reduced and do not reach more than two chord lengths across the span. These observations are in qualitative agreement with similar experiments on cylinders by Slaouti & Gerrard (1981).

Vortex coherence and alignment was verified by orienting the DPIV data plane in the spanwise direction. At the mid-span, vortices correlate well (no filament distortion) with the foil motion and remain stable and aligned with the span in excess of one wavelength into the wake. The flow is nearly two-dimensional except for spanwise flow in the vortex cores, in agreement with the results by Pineau *et al.* (1992) and Polidori *et al.* (1992).

6. Conclusions

Optimum propulsive performance of a harmonically oscillating foil is obtained after a parametric search which is aided by a careful consideration of the principal mechanisms governing the dynamics of its wake. Conditions for optimal production of thrust are:

- operation at Strouhal number between 0.25 and 0.40;
- large amplitude of heave motion-to-chord ratio (of order one);
- large maximum angle of attack, between 15° and 25° ;
- phase angle between heave and pitch (pitch leading heave) of about 75° when the reference point for heave motion is at the one-third chord length from the leading edge.

High efficiency accompanied by a thrust coefficient of order one is obtained at high Strouhal numbers S_{TE} , in the range of 0.3 to 0.4. The maximum measured efficiency in the present set of experiments was 87%.

Visualization experiments show that high efficiency accompanied by significant thrust development is associated with the generation of moderately strong leading-edge vortices, which subsequently amalgamate with trailing-edge vorticity leading to the formation of a reverse Kármán street. The phase angle between the heave and pitch motion is of critical importance, because it determines the timing of the formation and shedding of the leading-edge vortex, the optimal value for a pivot point of $b^* = \frac{1}{3}$ being at about 75° . Average thrust estimates based on the DPIV data (Reynolds number 1100) confirm the trends established by the force and power experiments at Reynolds number 40 000.

The impetus for the research on oscillating foils has been provided by observations on fish performance, which in many cases has been found to be outstanding. Here we can only confirm a single fact, which has been anticipated by fish biologists, i.e. that fish tails can be very efficient propulsors, reaching efficiencies above 85%. Bose & Lien (1989) predicted an 85% efficiency for the fin of a whale's flukes, on the basis of measurements on whales, and using linear theory with corrections for three-dimensional, viscous and large-amplitude effects. The present experiments show not only that this efficiency is feasible, but that it is achieved while producing substantial thrust.

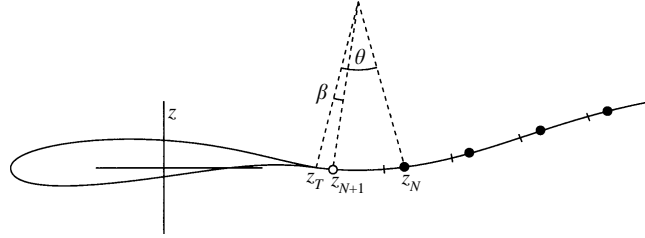


FIGURE 18. Vortex shedding algorithm.

Financial support of the Office of Naval Research, under contracts N00014-94-1-0735 and N00014-96-1-1141, monitored by P. Purtell, T. McMullen and J. Fein, and the Sea Grant Program under Grant Number NA46RG0434 is gratefully acknowledged.

Appendix. Description and verification of the numerical solution technique

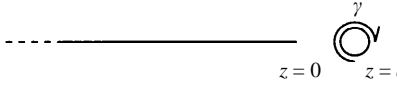
The numerical method used simulates the ideal two-dimensional flow around a Joukowski foil in arbitrary motion assuming that the wake consists of point vortices. The complex potential $w(z)$ is found through the conformal mapping $z = F(\zeta)$, given the velocity components of the foil and locations of all the vortices; z is a coordinate system coincident with the foil, and ζ is a transform plane where the foil profile is mapped to a circle. F is the Joukowski transform. The vortices convect with velocities given by Routh's rule (Sarpkaya 1989)

$$\frac{d\bar{z}_k}{dt} = \frac{1}{F'(\zeta_k)} \frac{d}{d\zeta} [w(\zeta) - i\gamma_k \log(\zeta - \zeta_k)]_{\zeta=\zeta_k} - \frac{i\gamma_k}{2} \frac{F''(\zeta_k)}{[F'(\zeta_k)]^2},$$

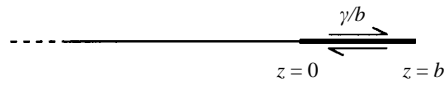
where $z_k = F(\zeta_k)$ is the location of a vortex and $2\pi\gamma_k$ its clockwise circulation. This expression is used to step forward the simulation in a second-order Runge–Kutta scheme. As shown by Streitlien & Triantafyllou (1995), the forces and moment that the foil experiences consist of added-mass terms and linear sums of all the vortices.

A critical element in such a method is the way in which new vortices are released near the trailing edge to form the wake behind the foil. We assume that the Kutta condition of finite flow velocity at the trailing edge applies, but this is not sufficient to uniquely specify the vortex shedding algorithm. A heuristic argument is introduced to determine both the strength and location of new vortices. For the Joukowski foil, matters are simplified in that vortices must leave the cusped trailing edge parallel to it. The vortex shedding algorithm, illustrated in figure 18, is based on Sarpkaya's (1975) method for bluff plates.

Within this algorithm, the location of a new vortex can be determined from an interpolation between the trailing edge and one or more previously shed vortices. Each vortex in the wake (solid dots) contains the circulation of a segment (between tick marks) of a continuous vortex sheet. The tick marks indicate material points that emanated at the trailing edge at the end of previous time steps. Figure 18 shows the situation at the end of the N th time step, when vortex $N+1$ is about to be introduced in the flow. A circular arc tangent to the trailing edge, z_T , is fitted through the known location of the previously shed vortex, z_N , with an arc angle θ . The new vortex will be placed on this arc, but with a smaller arc angle, β . To determine β we compare the flows due to a point vortex and a finite vortex sheet of the same circulation in the presence of a semi-infinite flat plate, as a simple model of the conditions near the trailing edge, figure 19.



$z=0$ $z=a$



$z=0$ $z=b$

$$\frac{dw}{dz} = \frac{i\gamma}{z-a} \left(\frac{a}{z}\right)^{1/2} = -\frac{i\gamma}{(az)^{1/2}} + O(z^{1/2})$$

$$\frac{dw}{dz} = \frac{-2i\gamma}{(bz)^{1/2}} + \frac{i\gamma}{b} \log \frac{z^{1/2}+b^{1/2}}{z^{1/2}-b^{1/2}} = -\frac{2i\gamma}{(bz)^{1/2}} + O(1)$$

FIGURE 19. Auxiliary problem to determine placement of the new vortex.

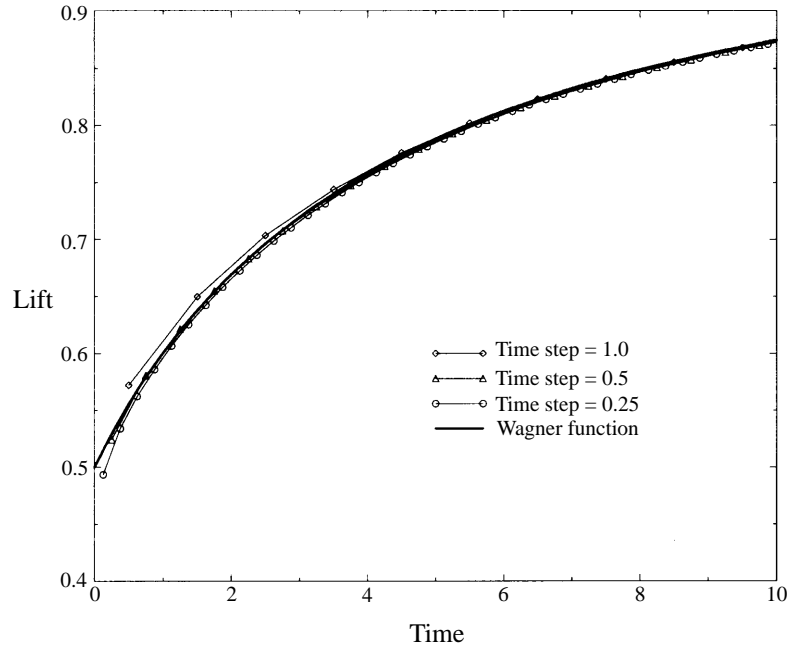


FIGURE 20. Force on impulsively started flat plate.

The complex velocities will have the same leading-order behaviour near $z = 0$ (the trailing edge) provided $a = b/4$, and this leads us to the choice $\beta = \theta/5$ in figure 18. With the location of the new vortex fixed, its strength is set to satisfy the Kutta condition. It is well known that the dynamics of a continuous vortex sheet cannot be predicted by the point-vortex discretization (Krasny 1987). Global quantities, however, such as forces and circulation are found to converge as the time step is reduced.

The lift force experienced by an impulsively started flat plate at 0.01 rad angle of attack is shown in figure 20, compared to the linear theory.

We see that the method converges to the Wagner function except for the initial moment, where lift is slightly under-predicted. The time scale is based on free-stream velocity and half-chord. A different test is shown in figure 21; here convergence in propulsive efficiency is presented for an oscillating flat plate.

We note that η converges to the linear result although only at a rate $(\text{time step})^{1/2}$. This is caused by the form of the local pressure distribution near the trailing edge. Furthermore, if we were to choose a different relation between β and θ , the method

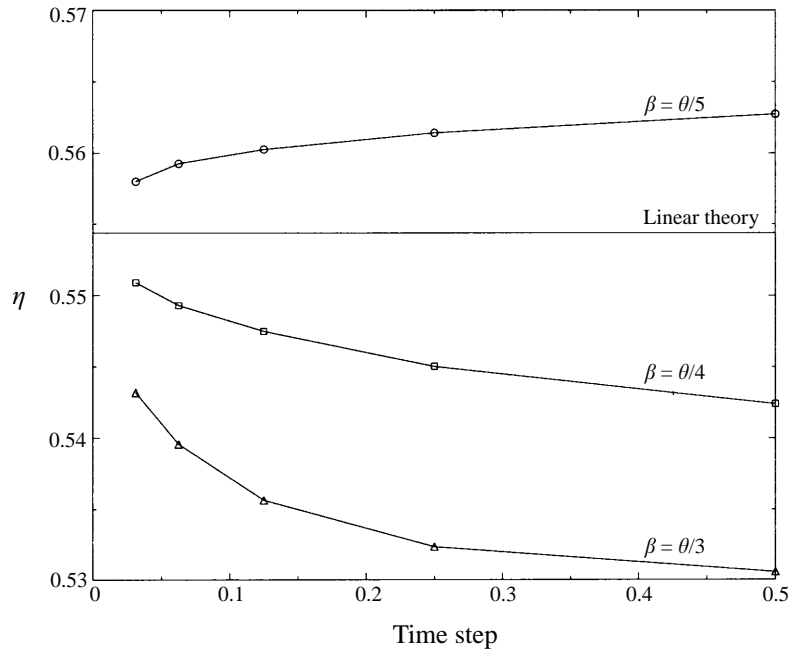


FIGURE 21. Efficiency for a flat plate heaving with amplitude 0.01 and period=6.

would still converge towards the desired result, but from below. It might be tempting to specify β somewhere between $\theta/5$ and $\theta/4$ to get perfect agreement with linear theory. However, there is no guarantee that this would yield more accurate result in nonlinear cases, and we have chosen to use the value $\theta/5$ in accordance with the argument above, expecting the error in η to be within 0.01 for a time step of 0.1. The results have proven to be insensitive to other chosen parameters, such as time integration scheme and finite-core vortices.

REFERENCES

- ANDERSON, J. M. 1996 Vorticity control for efficient propulsion. PhD Thesis, Joint Program, Massachusetts Institute of Technology & Woods Hole Oceanographic Institution.
- BATCHELOR, G. K. 1967 *An Introduction to Fluid Dynamics*. Cambridge University Press.
- BOSE, N. & LIEN, J. 1989 Propulsion of a fin whale (*Balaenoptera physalus*): why the fin whale is a fast swimmer. *Proc. R. Soc. Lond. A* **237**, 175–200.
- CHENG, H. K. & MURILLO, L. E. 1984 Lunate-tail swimming propulsion as a problem of curved lifting line in unsteady flow. Part 1. Asymptotic Theory. *J. Fluid Mech.* **143**, 327–350.
- DELAURIER, J. D. & HARRIS, J. M. 1982 Experimental study of oscillating wing propulsion. *J. Aircraft* **19** (5), 368–373.
- ELLINGTON, C. P. 1984 The aerodynamics of hovering insect flight. IV. Aerodynamic mechanisms. *Phil. Trans. R. Soc. Lond. B* **305**, 79–113.
- FREYMUTH, P. 1988 Propulsive vortical signature of plunging and pitching airfoils. *AIAA J.* **26**, 881–883.
- FREYMUTH, P. 1990 Thrust generation by an airfoil in hover modes. *Exps. Fluids* **9**, 17–24.
- GOPALKRISHNAN, R., TRIANTAFYLLOU, M. S., TRIANTAFYLLOU, G. S. & BARRETT D. S. 1994 Active vorticity control in a shear flow using a flapping foil. *J. Fluid Mech.* **274**, 1–21.
- GREYDANUS, J. H., VAN DE VOOREN, A. I. & BERGH, H. 1952 Experimental determination of the aerodynamic coefficients of an oscillating wing in incompressible, two-dimensional flow, parts I-IV. *National Luchtvaart-laboratorium, Amsterdam, Reports F-101, 102, 103 and 104.*

- KARPOUZIAN, G., SPEDDING, G. & CHENG, H. K. 1990 Lunate-tail swimming propulsion. Part 2. Performance analysis. *J. Fluid Mech.* **210**, 329–351.
- KATZ, J. 1981 A discrete vortex method for the non-steady separated flow over an airfoil. *J. Fluid Mech.* **102**, 315–328.
- KOOCHESFAHANI, M. 1989 Vortical patterns in the wake of an oscillating foil. *AIAA J.* **27**, 1200–1205.
- KRASNY, R. 1987 Computation of vortex sheet roll-up. In *Vortex Methods, Proc. UCLA Workshop*, Los Angeles (ed. C. Anderson & C. Greengard). Springer.
- LAI, P. S. K., BOSE, N. & MCGREGOR, R. C. 1993 Wave propulsion from a flexible-armed, rigid-foil propulsor. *Marine Technol.* **30** (1), 28–36.
- LIGHTHILL, J. 1975 *Mathematical Biofluidynamics*. SIAM.
- LONGVINOVICH, G. V. 1971 Hydrodynamics of a thin, flexible body. In *Hydrodynamic Problems in Bionics*, pp. 4–11. Joint Publications Research Service - 52605, Washington, DC, March 1971.
- MARESCA, C., FAVIER, D. & REBONT, J. 1979 Experiments on an airfoil at high angle of incidence in longitudinal oscillations. *J. Fluid Mech.* **92**, 671–690.
- MACCROSKEY, W. J. 1982 Unsteady airfoils. *Ann. Rev. Fluid Mech.* **14**, 285–311.
- MAXWORTHY, T. 1979 Experiments on the Weis–Fogh mechanism of lift generation by insects in hovering flight. Part 1. Dynamics of the fling. *J. Fluid Mech.* **93**, 47–63.
- MCCUNE, J. E. & TAVARES, T. S. 1993 Perspective: Unsteady wing theory - The Kármán/Sears legacy. *Trans. ASME Fluids Engng* **115**, 548–560.
- MCKENNA, S. 1996 DPIV resolution and uncertainty. Unpublished MIT Report.
- OHASHI, H. & ISHIKAWA, N. 1972 Visualization study of flow near the trailing edge of an oscillating airfoil. *Bull. JSME* **15** (85), 840–847.
- OHMI, K., COUTANCEAU, M., DAUBE, O. & LOC, T. P. 1991 Further experiments on vortex formation around an oscillating and translating airfoil at large incidences. *J. Fluid Mech.* **225**, 607–630.
- OHMI, K., COUTANCEAU, M., LOC, T. P. & DULIEU, A. 1990 Vortex formation around an oscillating and translating airfoil at large incidences. *J. Fluid Mech.* **211**, 37–60.
- OSHIMA, Y. & NATSUME, A. 1980 Flow field around an oscillating foil. In *Flow Visualization II, Proc. Second Intl Symp. on Flow Visualization, Bochum, Germany* (ed. W. Merzkirch), pp. 295–299. Hemisphere.
- OSHIMA, Y. & OSHIMA, K. 1980 Vortical flow behind an oscillating foil. *Proc. 15th IUTAM Intl Congress*, pp. 357–368. North Holland.
- PINEAU, G., TEXIER, A., COUTANCEAU, M. & LOC, T. P. 1992 Experimental and numerical visualization of the 3D flow around a short circular cylinder fitted with endplates. In *Flow Visualization VI* (ed. Y. Tanida & H. Miyashiro), pp. 343–347. Springer.
- POLIDORI, G., PINEAU, G., MERAIM, K. A. & COUTANCEAU, M. 1992 Shedding process of the initial vortices from impulsively started cylinders at $Re = 1000$: End and body geometry effects. In *Bluff Body Wakes, Dynamics and Instabilities* (ed. H. Eckelmann, J. M. R. Graham, P. Huerre, P. A. Monkewitz), pp. 285–288. Springer.
- PRANDTL, L. 1952 *Essentials of Fluid Dynamics*. New York: Hafner.
- REYNOLDS, W. C. & CARR, L. W. 1985 Review of unsteady, driven, separated flows. *AIAA Paper* 85-0527.
- SARPKAYA, T. 1975 An inviscid model of two-dimensional vortex shedding for transient and asymptotically steady separated flow over an inclined plate. *J. Fluid Mech.* **68**, 109–128.
- SARPKAYA, T. 1989 Computational methods with vortices – The 1988 Freeman scholar lecture. *Trans. ASME J. Fluids Engng* **111**, 5–52.
- SCHERER, J. O. 1968 Experimental and theoretical investigation of large amplitude oscillating foil propulsion systems. US Army Engineering Research and Development Laboratories.
- SLAOUTI, A. & GERRARD, J. H. 1981 An experimental investigation of the end effects on the wake of a circular cylinder towed through water at low Reynolds numbers. *J. Fluid Mech.* **112**, 297–314.
- STREITLIEN, K. & TRIANTAFYLLOU, M. S. 1995 Force and moment on a Joukowski profile in the presence of point vortices. *AIAA J.* **33**, 603–610.
- STREITLIEN, K., TRIANTAFYLLOU, G. S. & TRIANTAFYLLOU, M. S. 1996 Efficient foil propulsion through vortex control. *AIAA J.* **34**, 2315–2319.
- SZEPESY, S. & BEARMAN, P. W. 1992 Aspect ratio and end plate effects on vortex shedding from a circular cylinder. *J. Fluid Mech.* **234**, 191–217.

- TOKUMARU, P. T. & DIMOTAKIS, P. E. 1991 Rotary oscillation control of a cylinder wake. *J. Fluid Mech.* **224**, 77–90.
- TRIANAFYLLOU, M. S., TRIANAFYLLOU, G. S. & GOPALKRISHNAN, R. 1991 Wake mechanics for thrust generation in oscillating foils. *Phys. Fluids A* **3**, 2835–2837.
- TRIANAFYLLOU, G. S., TRIANAFYLLOU, M. S. & GROSENBAUGH, M. A. 1993 Optimal thrust development in oscillating foils with application to fish propulsion. *J. Fluids Struct.* **7**, 205–224.
- VISBALL, M. R. & SHANG, J. S. 1989 Investigation of the flow structure around a rapidly pitching foil. *AIAA J.* **27**, 1044–1051.
- WILLERT, C. E. & GHARIB, M. 1991 Digital particle image velocimetry. *Exps. Fluids* **10**, 181–193.
- WU, T. Y. 1961 Swimming of a waving plate. *J. Fluid Mech.* **10**, 321–344.
- WU, T. Y. 1971 Hydromechanics of swimming propulsion. Part 1. Swimming of a two dimensional flexible plate at variable forward speeds in an inviscid fluid. *J. Fluid Mech.* **46**, 337–355.